

# Physics-informed machine learning for reconstruction of dynamical systems with invariant measure score matching

Yongsheng Chen <sup>\*</sup>    Suddhasattwa Das <sup>†</sup>    Wei Guo <sup>‡</sup>    Xinghui Zhong <sup>§</sup>

January 21, 2026

## Abstract

In this paper, we develop a novel mesh-free framework, termed physics-informed neural networks with invariant measure score matching (PINN-IMSM), for reconstructing dynamical systems from unlabeled point-cloud data that captures the system's invariant measure. The invariant density satisfies the steady-state Fokker-Planck (FP) equation. We reformulate this equation in terms of its score function (the gradient of the log-density), which is estimated directly from data via denoising score matching, thereby bypassing explicit density estimation. This learned score is then embedded into a physics-informed neural network (PINN) to reconstruct the drift velocity field under the resulting score-based FP equation. The mesh-free nature of PINN allows the framework to scale efficiently to higher dimensions, avoiding the curse of dimensionality inherent in mesh-based methods. To address the ill-posed nature of high-dimensional inverse problems, we further recast the problem as a PDE-constrained optimization that seeks the minimal-energy velocity field. Under suitable conditions, we prove that this problem admits a unique solution that depends continuously on the score function. The constrained formulation is solved using a stochastic augmented Lagrangian method. Numerical experiments on representative dynamical systems, including the Van der Pol oscillator, an active swimmer in an anharmonic trap, chaotic Lorenz-63 and Lorenz-96 systems, demonstrate that PINN-IMSM accurately recovers invariant measures and reconstructs faithful dynamical behavior, successfully handling problems in up to five dimensions.

**Keywords:** Dynamical system learning, invariant measure, score matching, physics-informed neural networks (PINNs).

---

<sup>\*</sup>School of Mathematical Sciences, Zhejiang University, Hangzhou, 310027, China. 22035024@zju.edu.cn

<sup>†</sup>Department of Mathematics and Statistics, Texas Tech University, Lubbock, TX, 70409, USA. suddas@ttu.edu.

<sup>‡</sup>Department of Mathematics and Statistics, Texas Tech University, Lubbock, TX, 70409, USA. weimath.guo@ttu.edu.

<sup>§</sup>Corresponding author. School of Mathematical Sciences, Zhejiang University, Hangzhou, 310027, China. zhongxh@zju.edu.cn

# 1 Introduction

Reconstructing dynamical systems from observational data is a fundamental task across science and engineering, central to understanding and predicting complex phenomena from chaotic attractors and turbulent flows to pattern formation and neural activity. The problem involves finding a mathematical model, often parameterized in a trainable manner, such that its simulated behavior aligns with the observed data. Recent data-driven machine learning approaches have significantly advanced this field, providing flexible frameworks for systems with incomplete or noisy observations. Neural ordinary differential equations (ODEs) [1–4] and sparse identification of nonlinear dynamics (SINDy) [5–7] have proven effective for dynamical system identification. However, these methods adopt a Lagrangian perspective and rely heavily on accurate trajectory data to estimate derivatives, limiting their applicability when temporal information is sparse or unavailable. A scenario for recovering unknown dynamical systems from data with missing time labels was considered in [8], where the data are assumed to lie on a one-dimensional manifold. Their method minimizes the sliced-Wasserstein distance between samples generated by neural ODEs and training data, employing a trajectory segmentation technique to facilitate training. Nevertheless, the approach remains Lagrangian and is limited to lower-dimensional manifolds.

In this paper, we focus on the scenario where observational data are provided as a point cloud consisting of samples from an underlying dynamical system, but lack reliable temporal labels due to slow or unrecorded sampling. Such data frequently appear in fields including molecular dynamics, biology, healthcare, medical research, and numerical weather prediction. For dynamical systems, the distribution of states converges over time to a time-independent limit known as *invariant measure*. The observational data, though devoid of explicit timing, provides an empirical approximation of this invariant measure, which in turn encodes key information about the system’s dynamic law. Classical Lagrangian methods, which rely on time-labeled trajectories to estimate derivatives, are ineffective in this label-deficient setting.

To address the challenge, an Eulerian approach has been developed in [9, 10] to learn the dynamics from such data. This approach formulates the reconstruction as a partial differential equation (PDE) inverse problem, which infers the unknown velocity field directly from data by imposing the steady-state Fokker–Planck (FP) equation as a physical constraint, thereby circumventing the need for time-labeled trajectories. The method proceeds in three steps. First, the invariant density is approximated empirically by binning the data into a histogram  $\rho^*$ . This invariant density is known to satisfy the steady-state FP equation. Second, a finite volume scheme is employed to compute the solution  $\rho(v(\theta))$  of the FP equation, for a velocity field  $v(\theta)$ , which is parameterized by a neural network with trainable parameters  $\theta$ . Third,  $v(\theta)$  is optimized using a gradient-based method to minimize the loss function  $\mathcal{J}(\theta) := \mathcal{D}(\rho(v(\theta)), \rho^*)$ , where  $\mathcal{D}$  denotes a metric or divergence between probability measures. This framework has been validated on several benchmark examples. However, because it relies on a mesh-based PDE solver, it suffers from the curse of the dimensionality and is practically limited to problems of low dimensions ( $d \leq 3$ ).

The practical scalability of the aforementioned mesh-based Eulerian method is limited by their reliance on mesh-based discretization and the need to repeatedly solve the governing PDE, which becomes computationally prohibitive in higher dimensions. This limitation has motivated the development of mesh-free learning paradigms that encode the governing PDE structure directly within neural network parameterizations while maintaining differentiability for gradient-based optimization. Physics-informed neural networks (PINNs) [11–15] provide one such frame-

work by embedding the equations as soft or hard constraints in the training loss, enabling parameter/field identification without an explicit mesh-based PDE solver. Another direction is to use deep operator networks, such as DeepONet [16], Fourier neural operators [17], and graph neural operators [18], which learn mappings between function spaces to recover unknown parameters from observational data. While powerful, these operator methods typically demand large volumes of high-quality training data [19, 20]. Recent works that incorporate PDE constraints into such operator-learning frameworks, aim to reduce data requirements and enhance generalization capabilities [21, 22].

Motivated by the limitations of existing methods, we propose a novel mesh-free framework termed *PINN with invariant measure score matching* (PINN-IMSM), designed to reconstruct dynamical systems from data without explicit temporal labels. A key step is to reformulate the stationary FP equation in terms of the score function, i.e., the gradient of the log-density of the invariant measure, yielding a score-based stationary FP equation. PINN-IMSM first uses denoising score matching [23, 24] to learn this score function directly from unlabeled observational data, avoiding explicit density estimation. The learned score is subsequently embedded into a PINN to reconstruct the underlying velocity field by enforcing the physics constraint derived from the score-based FP equation.

To overcome the ill-posedness challenge in the standard PINN approach, we further formulate the reconstruction as a PDE-constrained optimization problem, seeking the minimal-energy velocity field that satisfies the FP equation. We prove that, under suitable conditions, this PDE-constrained optimization problem admits a unique solution, and that the solution is continuous with respect to the score function. This constrained formulation is solved efficiently via the stochastic augmented Lagrangian method [25]. Numerical experiments demonstrate that the proposed PINN-IMSM method achieves accurate and stable reconstruction of dynamical systems from observational data, successfully handling problems in dimensions up to five, thereby significantly surpassing the scalability of existing mesh-based and trajectory-based methods.

The remainder of this paper is organized as follows. In Section 2, we introduce background on stochastic differential equations, invariant measures, the FP equations, and the score estimation and PINNs. Section 3 is devoted to the details of the proposed PINN-IMSM framework. Section 4 presents numerical results validating the method’s performance and robustness. Conclusions and directions of future work are discussed in Section 5.

## 2 Background

### 2.1 Stochastic differential equations, invariant measures, and Fokker-Planck equations

Consider the stochastic differential equation (SDE) of the form

$$dX_t = v(X_t) dt + \Gamma(X_t) dW_t, \quad (2.1)$$

where  $X_t$  is a  $d$ -dimensional stochastic process with the state space  $\Omega \subset \mathbb{R}^d$  being a bounded Lipschitz domain,  $v : \Omega \rightarrow \mathbb{R}^d$  is the drift velocity,  $W_t$  is a standard  $m$ -dimensional Brownian motion, and  $\Gamma : \Omega \rightarrow \mathbb{R}^{d \times m}$  is the  $d \times m$ -dimensional diffusion coefficient matrix. We assume  $v$  and

$\Gamma$  are Lipschitz continuous. The solution to (2.1) is given by the integral equation:

$$X_t = X_0 + \int_0^t \mathbf{v}(X_s) \, ds + \int_0^t \Gamma(X_s) \, dW_s.$$

If the initial condition  $X_0$  is random with a probability density  $\rho_0$ , then the SDE induces a flow of probability densities  $\rho(\mathbf{x}, t)$ . The evolution of this density is governed by the FP equation [26–28]

$$\frac{\partial \rho(\mathbf{x}, t)}{\partial t} = -\nabla \cdot (\rho(\mathbf{x}, t) \mathbf{v}(\mathbf{x})) + \nabla \cdot (\nabla \cdot (\Sigma(\mathbf{x}) \rho(\mathbf{x}, t))) \triangleq \mathcal{F}\rho(\mathbf{x}, t), \quad (2.2)$$

with the initial condition  $\rho(\mathbf{x}, 0) = \rho_0(\mathbf{x})$  and the constraints:

$$\rho(\mathbf{x}, t) \geq 0, \quad \int_{\Omega} \rho(\mathbf{x}, t) \, d\mathbf{x} = 1. \quad (2.3)$$

Here,  $\mathcal{F}$  is the FP operator, and  $\Sigma$  is the diffusion coefficient matrix with its entries given by

$$\Sigma_{i,j}(\mathbf{x}) := \frac{1}{2} \left[ \Gamma(\mathbf{x}) \Gamma(\mathbf{x})^T \right]_{i,j} = \frac{1}{2} \left\langle \Gamma_i(\mathbf{x}), \Gamma_j(\mathbf{x}) \right\rangle_{\mathbb{R}^m},$$

where  $\Gamma_i(\mathbf{x})$  denotes the  $i$ -th row of the matrix  $\Gamma(\mathbf{x})$ . The matrix  $\Sigma$  is symmetric and positive semi-definite. To ensure probability conservation within  $\Omega$ , FP equation (2.2) is supplemented with homogeneous Neumann (reflecting) boundary conditions:

$$(-\mathbf{v}(\mathbf{x})\rho(\mathbf{x}, t) + \nabla \cdot (\Sigma(\mathbf{x})\rho(\mathbf{x}, t))) \cdot \mathbf{n}(\mathbf{x}) = 0, \quad \mathbf{x} \in \partial\Omega, \quad (2.4)$$

where  $\mathbf{n}(\mathbf{x})$  is the outward unit normal to  $\partial\Omega$ .

A density  $\rho(\mathbf{x})$  is stationary or invariant if it remains unchanged under this transformation, i.e.,  $\mathcal{F}\rho = 0$  subject to the constraints (2.3). This represents a statistical equilibrium that balances the deterministic drift and stochastic diffusion. Furthermore, an invariant density  $\rho$  defines an invariant probability measure  $\mu$  on the phase space by  $\mu(U) = \int_U \rho(\mathbf{x}) \, d\mathbf{x}$  for any measurable set  $U \subset \Omega$ . This measure is invariant in the sense that if  $X_0$  is distributed according to  $\mu$ , then  $X_t$  is also distributed according to  $\mu$  for all  $t > 0$ . Thus, the probability of the process being in any set  $U$  remains constant over time. The determination of these stationary densities is of significant practical importance, as they directly identify high- and low-probability regions in the phase space.

In this paper, we focus on the scenario of constant, isotropic diffusion, where the diffusion matrix takes the form  $\Sigma(\mathbf{x}) = DI$ , where  $D$  is a positive constant known as the diffusion coefficient, and  $I$  is the identity matrix. Consequently, the general SDE (2.1) simplifies to

$$dX_t = \mathbf{v}(X_t) \, dt + \sqrt{2D} \, dW_t, \quad (2.5)$$

which represents a dynamical system driven by isotropic white noise of strength  $D$ . In the zero-noise limit  $D \rightarrow 0^+$ , the system reduces to the continuity equation modeling the probability flow of the ODE given by  $\dot{\mathbf{x}} = \mathbf{v}(\mathbf{x})$ . For systems exhibiting stochastic stability [29–31], the invariant measure depends continuously on the noise level. This property, while difficult to establish theoretically, is widely observed empirically. For such systems, the constant isotropic diffusion model ensures the stationary distribution remains close to that of the noise-free counterpart.

The corresponding FP equation (2.2) then simplifies to

$$\frac{\partial \rho(\mathbf{x}, t)}{\partial t} = -\nabla \cdot (\rho(\mathbf{x}, t)\mathbf{v}(\mathbf{x})) + D\nabla^2 \rho(\mathbf{x}, t), \quad \mathbf{x} \in \Omega, \quad (2.6)$$

associated with the boundary condition

$$(\mathbf{D}\nabla \rho - \rho \mathbf{v}) \cdot \mathbf{n} = 0 \quad \text{on } \partial\Omega. \quad (2.7)$$

Under certain conditions [26], the invariant density  $\rho(\mathbf{x})$  of (2.6) exists and satisfies

$$\nabla \cdot (\rho(\mathbf{x})\mathbf{v}(\mathbf{x})) = D\nabla^2 \rho(\mathbf{x}), \quad \mathbf{x} \in \Omega. \quad (2.8)$$

This formulation implies that if the invariant density  $\rho(\mathbf{x})$  can be estimated from data, the underlying velocity field  $\mathbf{v}$  can be reconstructed by solving the inverse problem defined by (2.8). Our proposed method is developed within this paradigm.

## 2.2 Score estimation

The inverse problem posed by Equation (2.8) requires an accurate estimate of the invariant density  $\rho(\mathbf{x})$  from data. A critical first step is therefore to obtain a robust approximation of this invariant measure. In [10], this measure is approximated using the *occupation measure*, which is the empirical distribution obtained by binning observed points into histogram. However, this binning approach is well-known to suffer from the curse of dimensionality, rendering it impractical for high-dimensional problems [32]. To overcome this limitation, we employ *score matching* techniques, which have demonstrated remarkable success in high-dimensional density estimation [23, 24].

For any continuously differentiable probability density function  $\rho(\mathbf{x})$ , the associated score function  $\mathbf{s}(\mathbf{x})$  is defined as

$$\mathbf{s}(\mathbf{x}) = \nabla_{\mathbf{x}} \log \rho(\mathbf{x}). \quad (2.9)$$

Estimating the score function is often more tractable than direct density estimation, as it circumvents the computation of intractable normalizing constants [23, 24]. Moreover, the score function provides crucial information about the geometry of the underlying probability distribution and enables various downstream applications, including sample generation through Langevin Monte Carlo dynamics and gradient-based optimization procedures [33, 34].

A score network  $\mathbf{s}_\theta(\mathbf{x})$ , parameterized with trainable parameters  $\theta$ , is used to approximate the ground-truth score function  $\nabla_{\mathbf{x}} \log \rho(\mathbf{x})$ . The natural objective is to minimize the expected squared error  $\frac{1}{2}\mathbb{E}_{\rho(\mathbf{x})}\|\mathbf{s}_\theta(\mathbf{x}) - \nabla_{\mathbf{x}} \log \rho(\mathbf{x})\|_2^2$ , which defines the classical score matching framework [23]. However, this formulation cannot be applied directly because the true score function is unknown.

To overcome this challenge, numerous effective score matching variants have been developed in the literature. A widely used approach is denoising score matching [35], which has become a cornerstone technique in modern generative modeling. Given observed data  $\mathbf{x} \in \Omega$  from the unknown density  $\rho(\mathbf{x})$ , the main idea of the denoising score matching is to first perturb it with additive noise according to a conditional distribution  $p_\sigma(\tilde{\mathbf{x}}|\mathbf{x})$ , where  $\sigma$  controls the noise level. Score matching is then applied to estimate the score of the noise-perturbed distribution  $p_\sigma(\tilde{\mathbf{x}}) \triangleq \int_{\Omega} p_\sigma(\tilde{\mathbf{x}}|\mathbf{x})\rho(\mathbf{x})d\mathbf{x}$ . As proven in [35], this is equivalent to minimizing the objective:

$$\frac{1}{2}\mathbb{E}_{\rho(\mathbf{x})}\mathbb{E}_{p_\sigma(\tilde{\mathbf{x}}|\mathbf{x})}\left[\|\mathbf{s}_\theta(\tilde{\mathbf{x}}) - \nabla_{\tilde{\mathbf{x}}} \log p_\sigma(\tilde{\mathbf{x}}|\mathbf{x})\|_2^2\right], \quad (2.10)$$

where the expectation over  $\rho(\mathbf{x})$  is approximated using given data samples  $\mathbf{x}$ . The theoretical study in [35] ensures that, under appropriate regularity conditions, the optimal network  $\mathbf{s}_{\theta^*}(\mathbf{x})$  that minimizes this objective (2.10) satisfies

$$\mathbf{s}_{\theta^*}(\mathbf{x}) = \nabla_{\mathbf{x}} \log p_{\sigma}(\mathbf{x}), \quad \text{almost surely.} \quad (2.11)$$

When the noise level  $\sigma$  is sufficiently small such that  $p_{\sigma}(\tilde{\mathbf{x}}) \approx \rho(\tilde{\mathbf{x}})$ , the optimal score network yields a close approximation to the true score function:

$$\mathbf{s}_{\theta^*}(\mathbf{x}) = \nabla_{\mathbf{x}} \log p_{\sigma}(\mathbf{x}) \approx \nabla_{\mathbf{x}} \log \rho(\mathbf{x}).$$

Despite its theoretical appeal, the single-scale denoising approach in (2.10) often exhibits unsatisfactory performance in practice, particularly in low density regions where the signal-to-noise ratio is unfavorable [36]. This issue is addressed by the multi-scale denoising approach [36], which perturbs data with multiple noise levels and trains a single conditional score network to estimate scores across all noise scales simultaneously. This technique has since become a standard in score-based generative modeling.

The multi-scale denoising approach involves selecting a geometric sequence of noise scales  $\{\sigma_i\}_{i=1}^L$ , such that

$$\frac{\sigma_1}{\sigma_2} = \dots = \frac{\sigma_{L-1}}{\sigma_L} = \gamma > 1,$$

where  $\gamma$  is a fixed ratio. To determine the parameters of this sequence ( $\sigma_1$ ,  $\gamma$ , and  $L$ ), we follow the systematic approach proposed in [37], which is based on two criteria:

**Criterion 1.** Set the largest noise scale  $\sigma_1$  to the maximum pairwise Euclidean distance among all training data points. This ensures the Gaussian noise distribution at the largest scale adequately covers the entire support of the data.

**Criterion 2.** Choose the ratio  $\gamma$  such that it satisfies

$$\Phi(\sqrt{2d}(\gamma - 1) + 3\gamma) - \Phi(\sqrt{2d}(\gamma - 1) - 3\gamma) \approx 0.5,$$

where  $\Phi$  denotes the standard normal cumulative distribution function. This ensures sufficient overlap between consecutive noise levels for effective training.

The number of scales  $L$  is then chosen such that the smallest noise scale  $\sigma_L$  is above a threshold (typically  $\sigma_L \approx 0.01$ ), resulting in a well-conditioned noise sequence  $\{\sigma_i\}_{i=1}^L$ .

At each scale  $\sigma_i$ , the data is perturbed using a Gaussian distribution  $p_{\sigma_i}(\tilde{\mathbf{x}} | \mathbf{x}) = \mathcal{N}(\tilde{\mathbf{x}} | \mathbf{x}, \sigma_i^2 \mathbf{I})$ , yielding the noise-perturbed distribution  $p_{\sigma_i}(\tilde{\mathbf{x}}) \triangleq \int p_{\sigma_i}(\tilde{\mathbf{x}} | \mathbf{x}) \rho(\mathbf{x}) d\mathbf{x}$ . A single conditional score network  $\mathbf{s}_{\theta}(\mathbf{x}, \sigma)$  is then trained to jointly approximate the scores of all perturbed distributions, i.e.,  $\mathbf{s}_{\theta}(\mathbf{x}, \sigma_i) \approx \nabla_{\mathbf{x}} \log p_{\sigma_i}(\mathbf{x})$  for all  $i$ . For a fixed noise level  $\sigma_i$ , the denoising score matching objective derived from (2.10) is

$$\frac{1}{2} \mathbb{E}_{\rho(\mathbf{x})} \mathbb{E}_{p_{\sigma_i}(\tilde{\mathbf{x}} | \mathbf{x})} \left[ \left\| \mathbf{s}_{\theta}(\tilde{\mathbf{x}}, \sigma_i) + \frac{\tilde{\mathbf{x}} - \mathbf{x}}{\sigma_i^2} \right\|_2^2 \right].$$

These individual objectives are combined into a unified loss function for all noise scales:

$$\mathcal{L}_s = \frac{1}{2L} \sum_{i=1}^L \lambda(\sigma_i) \mathbb{E}_{\rho(\mathbf{x})} \mathbb{E}_{p_{\sigma_i}(\tilde{\mathbf{x}} | \mathbf{x})} \left[ \left\| \mathbf{s}_{\theta}(\tilde{\mathbf{x}}, \sigma_i) + \frac{\tilde{\mathbf{x}} - \mathbf{x}}{\sigma_i^2} \right\|_2^2 \right], \quad (2.12)$$

where  $\lambda(\sigma_i) > 0$  are scaling coefficients. Empirically, it is observed that  $\|\mathbf{s}_\theta(\mathbf{x}, \sigma)\|_2 \propto 1/\sigma$  for optimally trained networks [36], which motivates the choice  $\lambda(\sigma_i) = \sigma_i^2$  to balance the loss across scales. Substituting this weighting yields the final objective:

$$\mathcal{L}_s = \frac{1}{2L} \sum_{i=1}^L \mathbb{E}_{p(\mathbf{x})} \mathbb{E}_{p_{\sigma_i}(\tilde{\mathbf{x}}|\mathbf{x})} \left[ \left\| \sigma_i \mathbf{s}_\theta(\tilde{\mathbf{x}}, \sigma_i) + \frac{\tilde{\mathbf{x}} - \mathbf{x}}{\sigma_i} \right\|_2^2 \right]. \quad (2.13)$$

To facilitate learning across different noise scales and ensure numerical stability, we employ a parameterization of the conditional score network:  $\mathbf{s}_\theta(\mathbf{x}, \sigma) = \mathbf{s}_\theta(\mathbf{x})/\sigma$ , where  $\mathbf{s}_\theta(\mathbf{x})$  is an unconditional score network. This reparameterization mitigates the numerical instabilities that arise as  $\sigma \rightarrow 0$  [37], while the lower bound  $\sigma_L \approx 0.01$  provides additional regularization.

## 2.3 Physics-informed neural networks

This section reviews the framework of PINNs [11] for solving PDEs. PINNs provide a powerful, mesh-free alternative to traditional numerical methods, particularly for high-dimensional problems and complex geometries.

Consider a PDE of the general form

$$\mathcal{N}\mathbf{u}(\mathbf{x}) = \mathbf{f}(\mathbf{x}), \quad \mathbf{x} \in \Omega, \quad (2.14)$$

where  $\mathcal{N}$  is a nonlinear differential operator,  $\mathbf{u} : \mathbb{R}^d \rightarrow \mathbb{R}^m$  is the unknown solution field,  $\mathbf{f} : \mathbb{R}^d \rightarrow \mathbb{R}^m$  is a prescribed source function, and  $\Omega \subset \mathbb{R}^d$  is the computational domain. Traditional numerical methods, such as finite difference and finite element approaches, rely on spatial discretizations that can become computationally expensive for high-dimensional problems due to the curse of dimensionality [38, 39]. In contrast, PINNs [11] employ a neural network  $\hat{\mathbf{u}}(\mathbf{x}; \theta)$  to approximate the solution directly, where  $\theta$  denotes the collection of all trainable network parameters. The key innovation of PINNs is the incorporation of physical constraints into the training process via automatic differentiation [40], enabling the network to learn solutions that satisfy both the governing equations and available measurement data.

The framework utilizes two distinct point sets: observational data  $\{(\mathbf{y}_i, \mathbf{u}_i)\}_{i=1}^{N_u}$  (which may be sparse or absent) and collocation points  $\{\mathbf{x}_j\}_{j=1}^{N_f}$  sampled throughout the domain  $\Omega$ . The training process minimizes a composite physics-informed loss function:

$$\mathcal{L} = \omega_1 \mathcal{L}_{\text{data}} + \omega_2 \mathcal{L}_{\text{PDE}}, \quad (2.15)$$

with the data fidelity term

$$\mathcal{L}_{\text{data}} = \frac{1}{N_u} \sum_{i=1}^{N_u} \|\hat{\mathbf{u}}(\mathbf{y}_i; \theta) - \mathbf{u}_i\|_2^2,$$

and the physics-based residual term

$$\mathcal{L}_{\text{PDE}} = \frac{1}{N_f} \sum_{j=1}^{N_f} \|\mathcal{N}\hat{\mathbf{u}}(\mathbf{x}_j; \theta) - \mathbf{f}(\mathbf{x}_j)\|_2^2.$$

The weighting coefficients  $\omega_1$  and  $\omega_2$  balance contributions of data fitting and physics enforcement.

The optimization of the loss function (2.15) is typically performed using gradient-based algorithms such as the Adam optimizer [41] or L-BFGS [42], leveraging the automatic differentiation capabilities of modern deep learning frameworks. The trained network  $\hat{\mathbf{u}}(\mathbf{x}; \theta^*)$  provides a mesh-free approximation of the solution that can be evaluated at arbitrary points within the domain. Beyond forward problems, PINNs have demonstrated remarkable effectiveness in addressing inverse problems, where unknown parameters or functions in the governing equations are inferred from limited data [43–45]. In this work, we leverage this capability to address the challenging task of reconstructing unknown velocity  $\mathbf{v}$  in (2.8) from observed trajectory data.

### 3 PINN-IMSM: PINN with invariant measure score matching

This section introduce PINN-IMSM, a novel mesh-free machine learning framework that combines PINN with invariant measure score matching to reconstruct dynamical systems from noisy trajectory observations. The key innovation of PINN-IMSM lies in its ability to learn velocity fields without requiring explicit time labels, making it particularly suitable for real-world applications where temporal information is incomplete or unavailable. Our approach addresses three fundamental challenges in dynamical system reconstruction: (i) handling intrinsic noise in trajectory data, (ii) circumventing the curse of dimensionality inherent in traditional mesh-based methods, and (iii) ensuring well-posed reconstruction in high-dimensional spaces.

#### 3.1 Problem reformulation and method overview

The theoretical foundation of PINN-IMSM rests on utilizing the steady-state FP equation (2.8) as a forward model to characterize the invariant measure generated by the observed trajectories.

A central component of PINN-IMSM is the use of score functions rather than density functions for invariant measure estimation. We reformulate the steady-state FP equation (2.8) by substituting the score definition (2.9), yielding

$$\mathbf{s}(\mathbf{x}) \cdot \mathbf{v}(\mathbf{x}) + \nabla \cdot \mathbf{v}(\mathbf{x}) = D(|\mathbf{s}(\mathbf{x})|^2 + \nabla \cdot \mathbf{s}(\mathbf{x})), \quad \mathbf{x} \in \Omega. \quad (3.1)$$

In this formulation, the diffusion term serves a dual purpose: it accommodates intrinsic noise while preventing overfitting to noise components in the velocity field  $\mathbf{v}(\mathbf{x})$ , and simultaneously provides natural regularization. This approach distinguishes PINN-IMSM from existing mesh-based finite volume approaches [10] and enables the effective capture of complex dynamical behaviors in high-dimensional spaces.

Given trajectory measurements  $\{\tilde{X}_i\}_{i=1}^N$ , interpreted as samples from stochastic dynamical systems (2.1), PINN-IMSM reconstructs the associated velocity field  $\mathbf{v}(\mathbf{x})$  through a two-stage process:

- **Stage 1:** Train a score network  $\mathbf{s}_{\theta_1}(\mathbf{x}, \sigma_L)$  using denoising score matching to approximate the score function  $\mathbf{s}(\mathbf{x})$ .
- **Stage 2:** Reconstruct the velocity field  $\mathbf{v}(\mathbf{x})$  through a physics-informed approach based on Equation (3.1).

## 3.2 Score matching for invariant measures

The first stage of our methodology employs a noise-conditional score network  $s_{\theta_1}(\mathbf{x}, \sigma_L)$  to approximate the score function  $s(\mathbf{x}) = \nabla_{\mathbf{x}} \log \rho(\mathbf{x})$ , where  $\rho(\mathbf{x})$  is the density of the invariant measure and  $\theta_1$  denotes the trainable parameters. The network is trained using the multi-scale denoising score matching framework detailed in Section 2.2 by minimizing the loss function (2.13) across a well-conditioned geometric sequence of noise levels  $\{\sigma_i\}_{i=1}^L$ .

We treat the trajectory measurements  $\{\tilde{X}_i\}_{i=1}^N$  as time-agnostic samples from the invariant measure, forming the empirical distribution  $\widehat{\rho}_N := \frac{1}{N} \sum_{i=1}^N \delta_{\tilde{X}_i}$  on  $\Omega$ , where  $\delta_{\tilde{X}_i}$  denotes the Dirac mass at  $\tilde{X}_i$ . During training, we repeatedly sample data points  $\mathbf{x} \sim \widehat{\rho}_N$ , pick a noise level  $\sigma_i$  from the fixed noise sequence  $\{\sigma_i\}_{i=1}^L$ , and draw a standard Gaussian perturbation  $\xi \sim \mathcal{N}(\mathbf{0}, I_d)$ . For each pair  $(\mathbf{x}, \sigma_i)$  we then form the perturbed sample

$$\tilde{\mathbf{x}} = \mathbf{x} + \sigma_i \xi,$$

and assemble mini-batches of such triplets  $(\mathbf{x}, \tilde{\mathbf{x}}, \sigma_i)$  to evaluate and minimize the multi-scale denoising score matching loss (2.13).

The key insight is the selection of a sufficiently small smallest noise level  $\sigma_L$  such that the perturbed density approximates the density of the invariant measure, i.e.,  $p_{\sigma_L}(\mathbf{x}) \approx \rho(\mathbf{x})$ . This choice, combined with the theoretical guarantees of score matching (2.11), leads to the following approximation:

$$s_{\theta_1^*}(\mathbf{x}, \sigma_L) \approx \nabla_{\mathbf{x}} \log p_{\sigma_L}(\mathbf{x}) \approx \nabla_{\mathbf{x}} \log \rho(\mathbf{x}) = s(\mathbf{x}), \quad (3.2)$$

which provides PINN-IMSM with a robust estimate of the score function  $s(\mathbf{x})$  for the underlying dynamical system. To ensure compatibility with automatic differentiation in the subsequent physics-informed learning stage, the score network utilizes smooth activation functions, specifically the swish activation [46].

With the reliable estimate  $s_{\theta_1^*}(\mathbf{x}, \sigma_L) \approx s(\mathbf{x})$  obtained, we proceed to the second stage, which leverages the score-based reformulation (3.1) to recover the underlying velocity field.

## 3.3 PINN-based velocity field reconstruction

The second stage of PINN-IMSM constructs a neural network  $\mathbf{v}_{\theta_2}(\mathbf{x})$  parameterized by  $\theta_2$  to reconstruct the velocity field  $\mathbf{v}(\mathbf{x})$  using the score estimate obtained in the first stage.

### 3.3.1 The ill-posedness challenge in the standard PINN approach

We begin by reformulating Equation (3.1) in compact operator form:

$$\tilde{\mathcal{N}}(s(\mathbf{x}), \mathbf{v}(\mathbf{x})) = s(\mathbf{x}) \cdot \mathbf{v}(\mathbf{x}) + \nabla \cdot \mathbf{v}(\mathbf{x}) - D \left( |s(\mathbf{x})|^2 + \nabla \cdot s(\mathbf{x}) \right) = 0. \quad (3.3)$$

The standard PINN approach trains the neural network  $\mathbf{v}_{\theta_2}(\mathbf{x})$  by minimizing the physics-informed loss function over the trajectory measurements  $\{\tilde{X}_i\}_{i=1}^N$ :

$$\mathcal{L}_{PDE} = \frac{1}{N} \sum_{i=1}^N \|\tilde{\mathcal{N}}(s_{\theta_1^*}(\tilde{X}_i, \sigma_L), \mathbf{v}(\tilde{X}_i))\|_2^2, \quad (3.4)$$

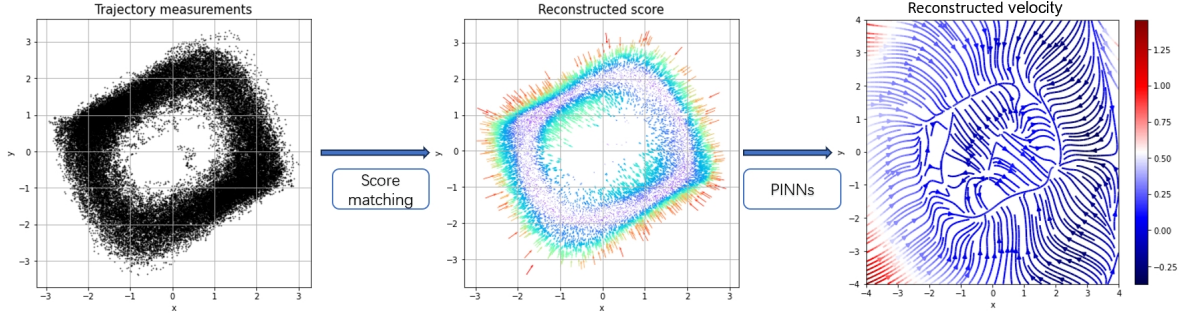


Figure 3.1: Velocity field reconstruction from trajectory data without explicit time labels. From trajectory measurements (left), we first reconstruct the score function via denoising score matching (middle). This reconstructed score is then integrated into the PINN framework to infer the velocity field across the state space (right).

where  $s_{\theta_1^*}(\tilde{X}_i, \sigma_L)$  is the pre-trained score estimate. The optimized network  $v_{\theta_2^*}(\mathbf{x})$  then approximates the velocity field  $v(\mathbf{x})$ , as illustrated in Figure 3.1.

Despite this straightforward formulation, the standard PINN approach faces several challenges. The primary issue is ill-posedness: Equation (3.1) may admit multiple velocity field solutions  $v(\mathbf{x})$  for a given score function  $s(\mathbf{x})$ , particularly in high-dimensional settings. Furthermore, the absence of explicit data-fitting terms in the loss function complicates optimization, making minimization of (3.4) particularly difficult [47, 48]. These limitations motivate our reformulation as a constrained optimization problem to ensure well-posedness and stability.

### 3.3.2 Ensuring well-posedness: PDE-constrained optimization approach

To address the ill-posedness of the velocity reconstruction problem identified in the previous section, we reformulate it as the following PDE-constrained optimization problem:

$$\begin{aligned} & \underset{v}{\text{minimize}} && \|v(\mathbf{x})\|^2 \\ & \text{subject to} && \tilde{N}(s(\mathbf{x}), v(\mathbf{x})) = 0, \end{aligned} \tag{3.5}$$

where  $\|v(\mathbf{x})\|^2 = \int_{\Omega} |v(\mathbf{x})|^2 d\mathbf{x}$ . This formulation selects the minimal-energy solution among all feasible solutions consistent with the score-based FP constraint.

The well-posedness of this constrained optimization approach is established by the following theorem. The required preliminaries including definitions of the relevant function spaces and norms, together with a complete proof are provided in Appendix A.

**Theorem 3.1** (Well-posedness of (3.5)). Assume  $s \in W^{1,\infty}(\Omega; \mathbb{R}^d)$  and that  $q_s = |s|^2 + \nabla \cdot s \geq 0$  almost everywhere in  $\Omega$ . Then the constrained optimization problem (3.5) admits a *unique* minimizer  $v^*$ . Moreover, the solution map  $s \mapsto v^*$  is locally Lipschitz with respect to the  $W^{1,\infty}$ -metric on  $s$  and the  $L^2$ -metric on  $v$ , i.e., there exist a neighborhood  $U$  of  $s$  and a constant  $C > 0$  such that, for any  $\tilde{s} \in U$ , the corresponding minimizer  $\tilde{v}^*$  satisfies

$$\|v^* - \tilde{v}^*\|_{L^2(\Omega)} \leq C \|s - \tilde{s}\|_{W^{1,\infty}(\Omega)}.$$

**Remark 3.1.** The condition  $q_s \geq 0$  is sufficient for the theorem. The conclusion remains valid under the weaker condition  $\|q_s^-\|_{L^\infty(\Omega)} < C_P^{-2}$ , where  $q_s^-(x) = \max\{-q_s(x), 0\}$  and  $C_P$  is the Poincaré constant for  $H_0^1(\Omega)$ .

This theorem guarantees that the minimal-energy solution exists, is unique, and depends continuously on the score function  $s$ . The Lipschitz continuity ensures that the reconstruction of the velocity field is stable with respect to perturbations in the score function. Specifically, if we approximate the true score  $s$  by an estimate  $\tilde{s}$  obtained from data (e.g., via score matching), the error in the reconstructed velocity field  $\|\mathbf{v}^* - \tilde{\mathbf{v}}^*\|_{L^2}$  is linearly controlled by the estimation error  $\|s - \tilde{s}\|_{W^{1,\infty}}$ . This provides a theoretical guarantee that an accurate score estimate leads to an accurate reconstruction of the underlying dynamics, which is crucial when the score is learned from finite samples.

In practice, we work with the data-driven surrogate of (3.5) obtained by replacing the true score  $s$  with its learned approximation  $s_{\theta_1^*}$ :

$$\begin{aligned} & \underset{\mathbf{v}}{\text{minimize}} \quad \|\mathbf{v}(\mathbf{x})\|^2 \\ & \text{subject to} \quad \tilde{\mathcal{N}}(\mathbf{s}_{\theta_1^*}(\mathbf{x}), \mathbf{v}(\mathbf{x})) = 0. \end{aligned} \tag{3.6}$$

Given that neural networks with smooth activation functions yield  $C^m$ -smooth approximations, the learned score function  $s_{\theta_1^*}(\mathbf{x}) \in C^m(\Omega)$  satisfies the regularity assumptions of Theorem 3.1. Thus, the surrogate problem (3.6) admits a unique solution  $\hat{\mathbf{v}}$  and enjoys Lipschitz stability. In particular, an  $\mathcal{O}(\varepsilon)$  error in  $s_{\theta_1^*}$  (measured in  $W^{1,\infty}$ ) leads to an  $\mathcal{O}(\varepsilon)$  error in the reconstructed velocity field (measured in  $L^2$ ). As learning improves  $s_{\theta_1^*}$  and the minimal-energy constraint regularizes residual high-frequency noise,  $\hat{\mathbf{v}}$  converges to the ideal solution  $\mathbf{v}^*$ .

The theoretical foundation for our approach leverages the Universal Approximation Theorem [49, 50], ensuring that neural networks with sufficiently smooth activation functions can approximate any smooth function with arbitrary precision. Thus, solving problem (3.6) using neural network architectures provides a robust computational approach to approximating the velocity field solution  $\mathbf{v}^*$ .

### 3.3.3 Numerical implementation: stochastic augmented Lagrangian method

With the well-posedness of the constrained optimization problem (3.6) established in Theorem 3.1, we now consider its numerical implementation using neural networks. Several approaches have been proposed for constrained learning in physics-informed settings including soft penalty methods [11], penalty-based hard constraint formulations [51], adversarial training frameworks [52], and stochastic augmented Lagrangian methods [25]. Among these, we adopt the stochastic augmented Lagrangian approach introduced in [25], originally developed for physics-constrained training of encoder-decoder networks to approximate the Fokker-Planck-Landau collision operator. This approach builds upon the classical augmented Lagrangian framework, originally known as the method of multipliers and first proposed by [53] and [54] for nonlinear constrained optimization problems.

We adapt the stochastic augmented Lagrangian approach to our score-based PDE-constrained optimization formulation (3.6). Rather than approximating a known physical operator while preserving conservation laws, we aim to reconstruct an unknown minimum-energy velocity field from unlabeled trajectory data through a PDE constraint involving a separately learned score function.

Specifically, the augmented Lagrangian approach reformulates the PDE-constrained optimization problem (3.6) into a sequence of unconstrained optimization problems indexed by  $k$ :

$$\underset{\theta_2}{\text{minimize}} \quad \mathcal{L}(\theta_2, \lambda_k, \mu_k), \quad (3.7)$$

with  $\mathcal{L}$  being the augmented Lagrangian merit function:

$$\mathcal{L}(\theta_2, \lambda_k, \mu_k) = \|\mathbf{v}_{\theta_2}\|^2 + \lambda_k \tilde{\mathcal{N}}(\theta_2) + \frac{\mu_k}{2} \|\tilde{\mathcal{N}}(\theta_2)\|^2, \quad (3.8)$$

where  $\lambda_k$  is the Lagrange multiplier and  $\mu_k$  is the augmented Lagrangian penalty factor. Here,  $\tilde{\mathcal{N}}(\theta_2) := \mathcal{N}(\mathbf{s}_{\theta_1^*}, \mathbf{v}_{\theta_2})$  denotes the PDE residual from (3.3), evaluated using the score estimate  $\mathbf{s}_{\theta_1^*}$  obtained in the first stage and the parameterized velocity field  $\mathbf{v}_{\theta_2}$ . We remark that for the constrained formulation, the original PINN loss (3.4) is no longer minimized directly. Instead, the physics residual appears as a constraint in (3.6), which is handled through the augmented Lagrangian framework in (3.7)-(3.8).

The stochastic augmented Lagrangian method employs a two-level nested loop structure: the inner loop uses stochastic gradient descent (SGD) to solve the unconstrained optimization problem (3.7), while the outer loop updates Lagrange multipliers and penalty parameters in (3.8).

**Inner-loop optimization via stochastic gradient descent** We solve the unconstrained optimization problem (3.7) using mini-batch SGD, adapting the approach from [25] to our PDE-constrained setting.

Classical augmented Lagrangian methods solve the inner optimization problem (3.7) to a gradient-norm tolerance  $w_k$ , i.e.,

$$\|\nabla_{\theta_2} \mathcal{L}(\theta_{2,k}, \lambda_k, \mu_k)\|_2 \leq w_k, \quad (3.9)$$

with  $w_k$  gradually tightened as the algorithm converges toward the constrained solution. However, this criterion is impractical in stochastic settings for two reasons: first, accurately estimating the optimality norm  $\|\nabla_{\theta_2} \mathcal{L}\|_2$  is infeasible with stochastic mini-batch gradients; second, gradient norms do not serve as meaningful termination criteria in machine learning, where prediction accuracy of the neural network is the primary objective.

Instead of checking convergence via gradient norms, the SGD algorithm is configured to iterate through the entire training dataset once per outer-loop iteration. This yields a fixed number of SGD iterations in each inner loop:

$$N_{\text{iter}} = \frac{N}{N_b}, \quad (3.10)$$

where  $N$  is the training dataset size, and  $N_b$  is the batch size. We further introduce a user-specified parameter  $N_{\text{aug}}$  that controls the number of outer iterations performed for each random permutation of the training dataset. This enables multiple optimization passes over identical datasets and batches before new random batches are generated, with each pass solving a distinct inner optimization problem characterized by updated Lagrange multiplier  $\lambda_k$  and penalty factor  $\mu_k$ .

**Outer-loop updating of multipliers and penalties** We update the Lagrange multiplier  $\lambda_k$  and penalty parameter  $\mu_k$  in the outer loop based on the progress of inner-loop optimization. Traditional

augmented Lagrangian methods employ dynamic constraint tolerances to guide these updates, presupposing that each inner optimization problem consistently achieves the required dynamic tolerance. However, since our inner-loop solves the optimization problem via SGD with a fixed number of iterations, such convergence cannot be guaranteed.

We adopt a criterion based on sufficient reduction in PDE constraint violation, following the approach in [25]. Specifically, the multiplier is updated when the current PDE residual shows sufficient improvement relative to the best value recorded thus far:

$$\|\tilde{\mathcal{N}}(\theta_2^{k+1})\|_2 \leq \eta \|\tilde{\mathcal{N}}_{\text{best}}\|_2, \quad (3.11)$$

where  $\eta \in (0, 1)$  is a reduction factor and  $\tilde{\mathcal{N}}_{\text{best}}$  tracks the smallest PDE residual achieved during training. When this condition is satisfied, the multiplier follows the standard update:

$$\lambda_{k+1} = \lambda_k + \mu_k \tilde{\mathcal{N}}(\theta_2^{k+1}). \quad (3.12)$$

Otherwise, the penalty parameter is increased:

$$\mu_{k+1} = \min(a\mu_k, \mu_{\text{max}}), \quad (3.13)$$

where  $a > 1$  is a scalar parameter, and  $\mu_{\text{max}}$  is an upper bound to prevent numerical instability.

We end this subsection by summarizing the complete stochastic augmented Lagrangian algorithm. First, we specify the number of random permutations of the training dataset,  $N_{\text{shuffle}}$ . Then, for each permutation, we perform  $N_{\text{aug}}$  outer iterations; each outer iteration consists of:

- **Inner loop:**  $N_{\text{iter}}$  SGD updates of the neural network parameters  $\theta_2$ .
- **Outer update:** Update the Lagrange multipliers and penalty terms based on the constraint satisfaction criterion (3.11).

### 3.4 Summary of the PINN-IMSM framework

Algorithm 1 outlines the complete PINN-IMSM procedure for reconstructing the velocity field  $v(\mathbf{x})$  from the score-based formulation (3.1). The method proceeds in two sequential stages, using only the trajectory measurements  $\{\tilde{X}_i\}_{i=1}^N$  as training data:

- **Stage 1 (score estimation):** The score network  $s_{\theta_1}(\mathbf{x})$  is trained on the trajectory data by minimizing the multi-scale denoising score matching objective (2.13). This yields the approximation  $s_{\theta_1^*}(\mathbf{x}, \sigma_L) \approx s(\mathbf{x}) = \nabla_{\mathbf{x}} \log \rho(\mathbf{x})$ .
- **Stage 2 (velocity reconstruction):** With the pre-trained score estimate  $s_{\theta_1^*}$  fixed, the velocity network  $v_{\theta_2}(\mathbf{x})$  is trained using the same trajectory data. This is achieved by solving the PDE-constrained optimization problem (3.6) via the stochastic augmented Lagrangian framework. The solution to this problem inherently satisfies the physics constraint (3.1) and, by Theorem 3.1, corresponds to the unique minimum  $L^2$ -norm velocity field.

**Remark on implementation** In Stage 2, the stochastic augmented Lagrangian method introduces several hyperparameters, such as  $\eta$  and  $a$ . However, the training results remain relatively insensitive to their specific choices. This is due to the dynamic update of the Lagrange multiplier and penalty factor, governed by the convergence metric (3.11). Moreover, the augmented Lagrangian merit function (3.8) is easier to optimize compared to the direct PDE loss (3.4), thereby helping to mitigate common training difficulties encountered in standard PINN formulations. Numerical results in Section 4 show that this approach consistently achieves smaller PDE residuals than the standard PINN method.

The logical flow of the overall PINN-IMSM pipeline is summarized in Figure 3.2.

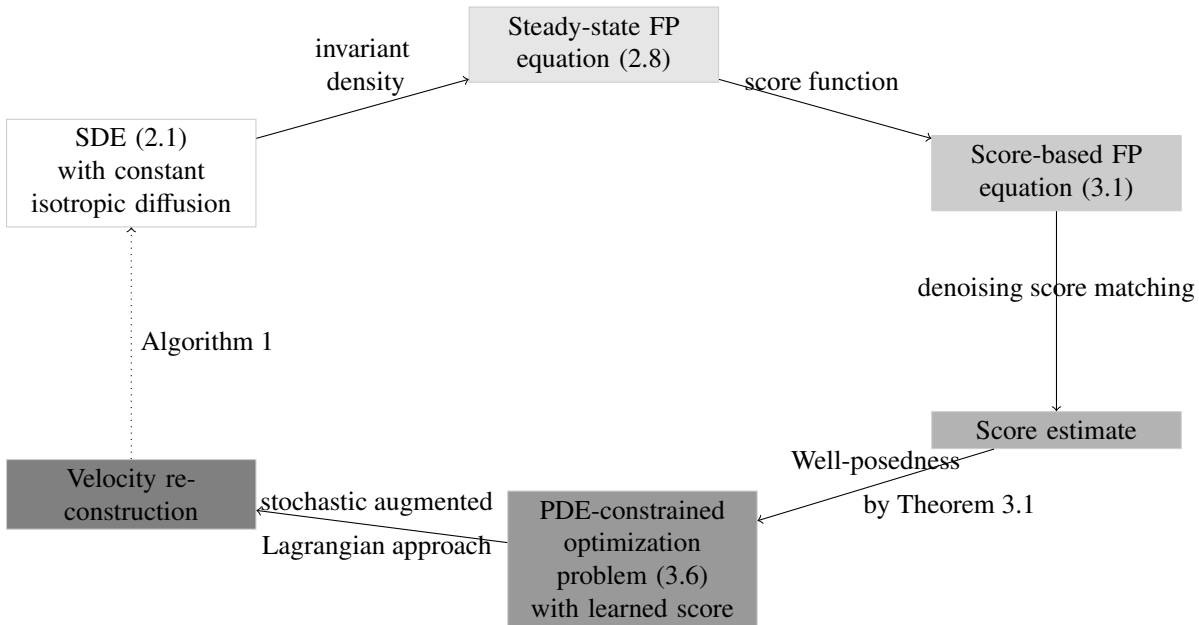


Figure 3.2: Schematic outline of the PINN-IMSM workflow. The goal is to reconstruct the drift term of an SDE from unlabeled trajectory data by combining invariant measure score matching with PINNs. Starting from an SDE with constant isotropic diffusion, the framework transforms the problem into a steady-state FP equation, which is then reformulated using the score function of the invariant density. The method proceeds in two stages: first, estimating the score function via multi-scale denoising score matching; second, reconstructing the velocity field by solving a well-posed PDE-constrained optimization problem within the stochastic augmented Lagrangian framework.

## 4 Numerical results

This section presents numerical examples to demonstrate the performance of the proposed PINN-IMSM framework on several dynamical systems. The goal is to evaluate how well it can recover the underlying velocity field from noisy, unlabeled trajectory data.

The method employs two neural networks. The score network  $s_{\theta_1}$  is a six-layer multilayer perceptron (MLP) with 64 neurons per hidden layer, and the velocity network  $v_{\theta_2}$  is a six-layer MLP with 128 neurons per hidden layer. Both networks employ the Swish activation function [46]

---

**Algorithm 1** PINN-IMSM for velocity field reconstruction from unlabeled trajectory measurements.

---

**Require:** trajectory measurements  $\{\tilde{X}_i\}_{i=1}^N$ , maximum number of epochs  $K$  for the score network, update tolerance  $\eta$ , convergence tolerance  $\epsilon$ , initial penalty  $\mu_{\text{init}}$ , penalty update factor  $a$ , penalty upper bound  $\mu_{\text{max}}$ , batch size  $N_b$ , number of random shuffles  $N_{\text{shuffle}}$  and number of iterations per shuffle  $N_{\text{aug}}$ .

**Ensure:** *optimized score network parameter set*  $\theta_1^*$   
choose noise scales  $\{\sigma_i\}_{i=1}^L$ ; initialize  $\theta_1^0$  from normal distribution around zero.

**for**  $k = 1, 2, \dots, K$  **do**  
    compute the loss  $\mathcal{L}_s(\theta_1^{k-1})$  via (2.13)  
    update  $\theta_1^k \leftarrow \operatorname{argmin}_{\theta_1} \mathcal{L}_s(\theta_1)$   
**end for**

**Ensure:** *optimized velocity network parameter set*  $\theta_2^*$   
 $\lambda_0 \leftarrow 0$ ; initialize  $\theta_2^0$  from a normal distribution around zero; set  $\tilde{\mathcal{N}}_{\text{best}} \leftarrow \tilde{\mathcal{N}}(\theta_2^0)$   
**for**  $j = 1, 2, \dots, N_{\text{shuffle}}$  **do**  
    Randomly shuffle the training data and form batches of size  $N_b$   
     $\mu_0 \leftarrow \mu_{\text{init}} * (j + 1)$   
    **for**  $k = 1, 2, \dots, N_{\text{aug}}$  **do**  
        solve (3.8) using SGD  
        update  $\theta_2^k \leftarrow \operatorname{argmin}_{\theta_2} \left( \|\mathbf{v}(\theta_2)\|^2 + \lambda_{k-1}^T \tilde{\mathcal{N}}(\theta_2) + \frac{\mu_{k-1}}{2} \|\tilde{\mathcal{N}}(\theta_2)\|^2 \right)$   
        **if**  $\|\tilde{\mathcal{N}}(\theta_2^k)\|_2 \leq \eta \|\tilde{\mathcal{N}}_{\text{best}}\|_2$  **then**  
            **if**  $\|\tilde{\mathcal{N}}(\theta_2^k)\|_2 \leq \epsilon$  **then**  
                **Solution** found; terminate with  $\theta_2^* = \theta_2^k$   
            **end if**  
             $\lambda_k \leftarrow \lambda_{k-1} + \mu_{k-1} \tilde{\mathcal{N}}(\theta_2^k)$   
             $\tilde{\mathcal{N}}_{\text{best}} \leftarrow \tilde{\mathcal{N}}(\theta_2^k)$   
             $\mu_k \leftarrow \mu_{k-1}$   
        **else**  
             $\lambda_k \leftarrow \lambda_{k-1}$   
             $\mu_k \leftarrow \min(a * \mu_{k-1}, \mu_{\text{max}})$   
        **end if**  
    **end for**  
     $\lambda_0 \leftarrow \lambda_{N_{\text{aug}}}$   
**end for**

---

and are optimized using Adam [55]. These architectural choices, determined empirically, yield stable performance across all experiments.

For each example, the training data are generated by simulating the SDE (2.5), where the true drift velocity is given in the ODE form  $\dot{x} = v(x)$ , and the diffusion coefficient  $D$  controls the noise level. We integrate the SDE numerically using the Euler–Maruyama method: given a time step  $\Delta t$ , the trajectory is updated as

$$X_{j+1} = X_j + v(X_j)\Delta t + \sqrt{2D}\xi_j \sqrt{\Delta t}, \quad (4.1)$$

where  $\{\xi_j\}$  are independent standard normal random vectors in  $\mathbb{R}^d$ . From the resulting long-time simulations, we collect point samples to form the training dataset.

To visualize the results, we estimate the invariant density by simulating long-time trajectories (again with the Euler–Maruyama scheme) and binning the samples into a two-dimensional histogram. We report two density estimates: a *reference* density obtained from simulations using the true drift velocity and a *learned* density obtained from simulations using our reconstructed velocity field  $v_{\theta_2^*}$ . Most examples show the densities using hexagonal bins for a smooth visualization. For direct comparison with prior work [10], Example 4.1 employs rectangular bins. In all figures, “Aug\_lag” denotes PINN-IMSM implemented with the stochastic augmented Lagrangian method in Section 3.3.

**Example 4.1 (Van der Pol oscillator).** In this example, we consider the Van der Pol oscillator [56] with the drift velocity

$$\begin{cases} \dot{x} = y, \\ \dot{y} = c(1 - x^2)y - x, \end{cases} \quad (4.2)$$

where  $c = 0.5$ . The diffusion coefficient is set as  $D = 0.05$ .

Figure 4.1 compares the reference system (top row) with the PINN-IMSM reconstruction (bottom row). The top row displays the ground-truth velocity field (left), the corresponding reference invariant density (middle), and noisy trajectory samples that serve as the training data (right). The bottom row shows the results of the proposed PINN-IMSM method: the reconstructed velocity field  $v_{\theta_2^*}$  (left), the learned invariant density induced by this field (middle), and representative trajectories generated by Langevin dynamics driven by the learned score network  $s_{\theta_1^*}$  (right). The Langevin samples provide an independent check of the score estimation quality. We observe that the reconstructed velocity deviates from the ground-truth field in regions far from the attracting limit cycle, where trajectory data are sparse and the drift velocity is therefore weakly identified. However, these regions carry little probability mass under the invariant measure. Consequently, the learned dynamics still reproduce the invariant density with high fidelity in the high-probability region around the attracting set. This indicates that the PINN-IMSM method captures the correct long-time statistical structure even where the drift velocity is not tightly constrained in low-density, poorly sampled regions. Both densities use rectangular bins for direct comparison with [10]. Under this matched discretization, the learned invariant density agrees well with those in [10].

Figure 4.2 further compares the PDE residual during training for the standard PINN and the proposed PINN-IMSM (“Aug\_lag”). It can be observed that the proposed PINN-IMSM method achieves a much smaller residual, demonstrating the effectiveness of the stochastic augmented Lagrangian method in enforcing the physics constraint.

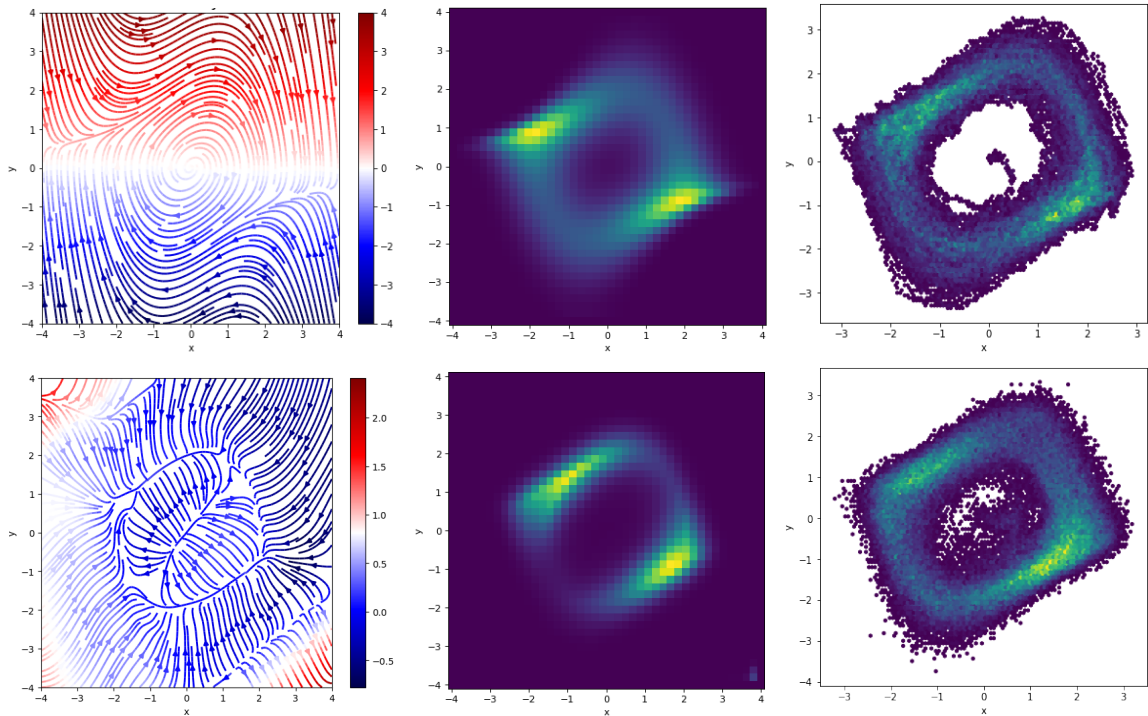


Figure 4.1: Van der Pol oscillator (4.2) with  $D = 0.05$ . **Top:** ground-truth velocity field (left), reference invariant density (middle), and noisy trajectory samples (right). **Bottom:** PINN-IMSM reconstructed velocity field  $v_{\theta_2^*}$  (left), learned invariant density (middle), and samples generated by Langevin dynamics from the learned score  $s_{\theta_1^*}$  (right).

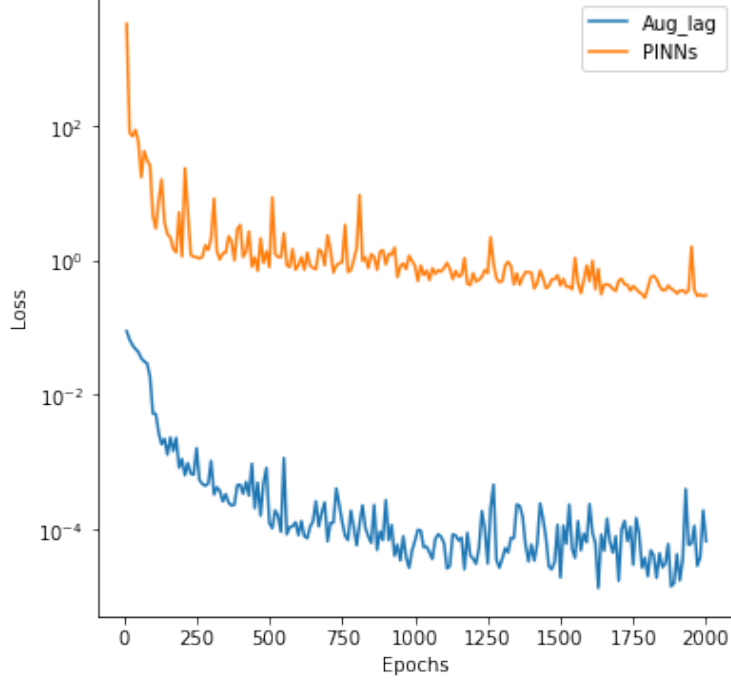


Figure 4.2: PDE residual during training for the standard PINN and PINN-IMSM (“Aug\_lag”) on the Van der Pol oscillator.

**Example 4.2 (Active swimmer in an anharmonic trap).** We consider a model from active matter describing the motion of a motile swimmer in an anharmonic trap [57]. The two-dimensional state  $(x, v)$  evolves with the drift velocity

$$\begin{aligned}\dot{x} &= -x^3 + v, \\ \dot{v} &= -\gamma v,\end{aligned}\tag{4.3}$$

where  $\gamma = 0.1$ , and the diffusion coefficient is set to  $D = 1.0$ .

Figure 4.3 compares the learned invariant density from the PINN-IMSM method with the reference density for the active swimmer system. For conciseness, we show only the density visualizations in this example. The close visual agreement demonstrates that the PINN-IMSM method captures the invariant statistics induced by the stochastically forced dynamics.

**Example 4.3 (Lorenz-63 system).** We consider the Lorenz-63 system [58], a canonical chaotic model. The drift velocity is given by

$$\begin{cases} \dot{x} = c_1(y - x), \\ \dot{y} = x(c_2 - z) - y, \\ \dot{z} = xy - c_3z, \end{cases}\tag{4.4}$$

where  $(c_1, c_2, c_3) = (10, 28, 8/3)$ . The diffusion coefficient is taken as  $D = 10$ .

The Lorenz-63 system presents a known challenge for the simultaneous reconstruction of all three velocity components. As noted in prior work [10], a learned velocity field may approximate the stationary state (i.e., satisfy the steady-state FP equation) yet fail to satisfy other physical

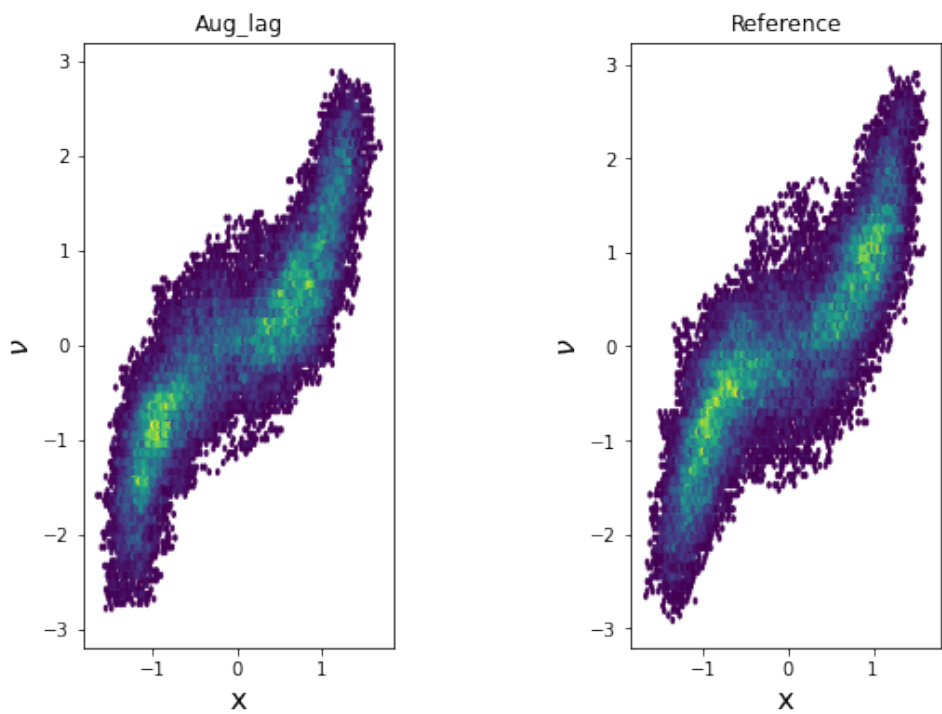


Figure 4.3: Invariant density estimates for the active swimmer model (4.3) with  $\gamma = 0.1$  and  $D = 1.0$ . **Left:** learned invariant density from the reconstructed velocity. **Right:** reference invariant density from the ground-truth velocity.

properties of the invariant measure. Whether this difficulty arises from inherent non-uniqueness in the inverse problem or simply inconvenient local minima during training remains an open question for future investigation.

Given this challenge, we evaluate the PINN-IMSM method on partial reconstructions. Figure 4.4 presents the results. The left column shows the ground-truth drift velocity field and the corresponding reference invariant density. The middle column shows a partial reconstruction where only  $\dot{x}$  is learned, with  $\dot{y}$  and  $\dot{z}$  treated as known. The right column further learns both  $\dot{x}$  and  $\dot{y}$ , again with  $\dot{z}$  treated as known. In all cases, the invariant density is visualized via the empirical occupation measure projected on the  $(x, z)$  plane. Following [9], the occupation measure is formed by randomly subsample trajectories, which confirms that the PINN-IMSM method remains applicable when measurement times are irregular or unavailable.

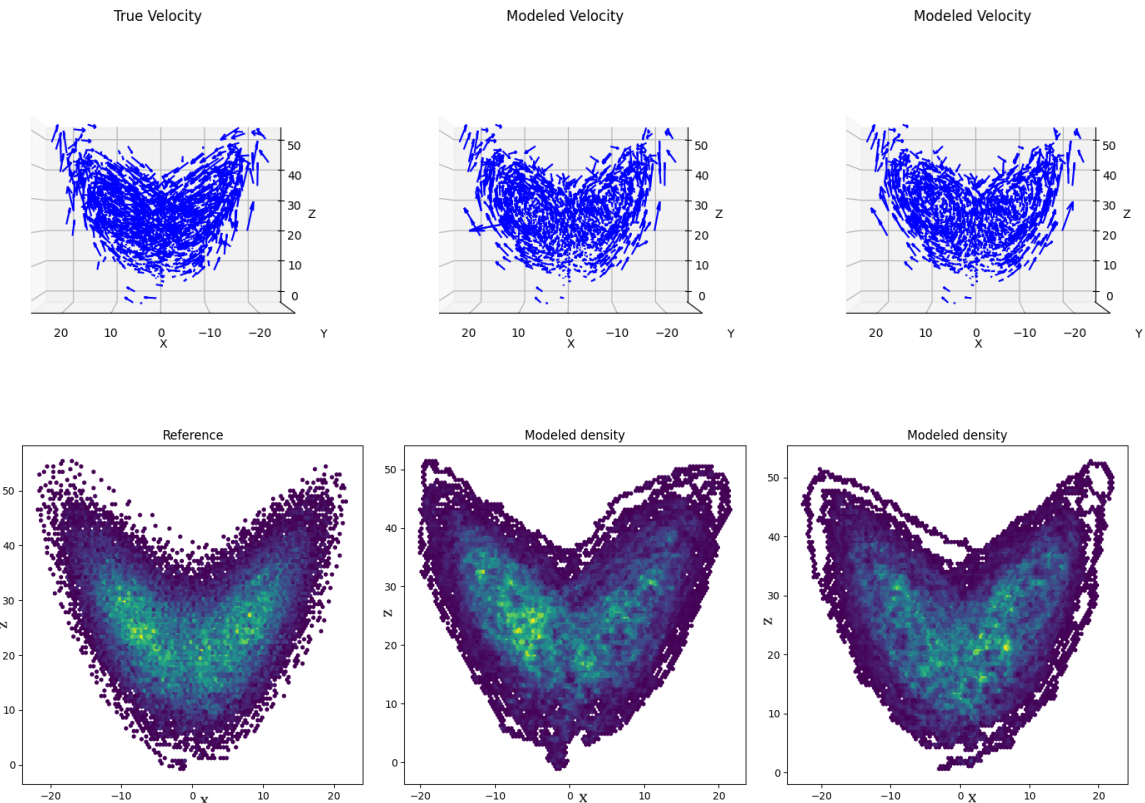


Figure 4.4: Lorenz-63 system (4.4) with  $D = 10$ . **Top:** ground-truth velocity field (left), reconstructed velocity learning only  $\dot{x}$  (middle), and reconstructed velocity learning  $\dot{x}$  and  $\dot{y}$  (right). **Bottom:** corresponding invariant densities on the  $(x, z)$  plane.

**Example 4.4 (Lorenz-96 system).** We examine the Lorenz-96 system [59, 60], defined for  $i = 1, \dots, N$  by

$$\frac{dx_i}{dt} = (x_{i+1} - x_{i-2})x_{i-1} - x_i + F, \quad (4.5)$$

with periodic indexing:  $x_{-1} = x_{N-1}$ ,  $x_0 = x_N$ , and  $x_{N+1} = x_1$ . Here  $F$  is a constant forcing term, the term  $-x_i$  represents linear damping, and the quadratic term models advection while conserving

kinetic energy in the absence of damping. We set  $N = 5$  and  $F = 8$ . The diffusion coefficient is  $D = 0.05$ .

Given the five-dimensional state space, we visualize the invariant density induced by the reconstructed drift velocity through two-dimensional projection histograms. Figure 4.5 shows representative projection densities, capturing the characteristic statistical structure of the chaotic attractor. These results demonstrate that the PINN-IMSM method is effective in higher-dimensional settings where mesh-based density solvers become computationally prohibitive.

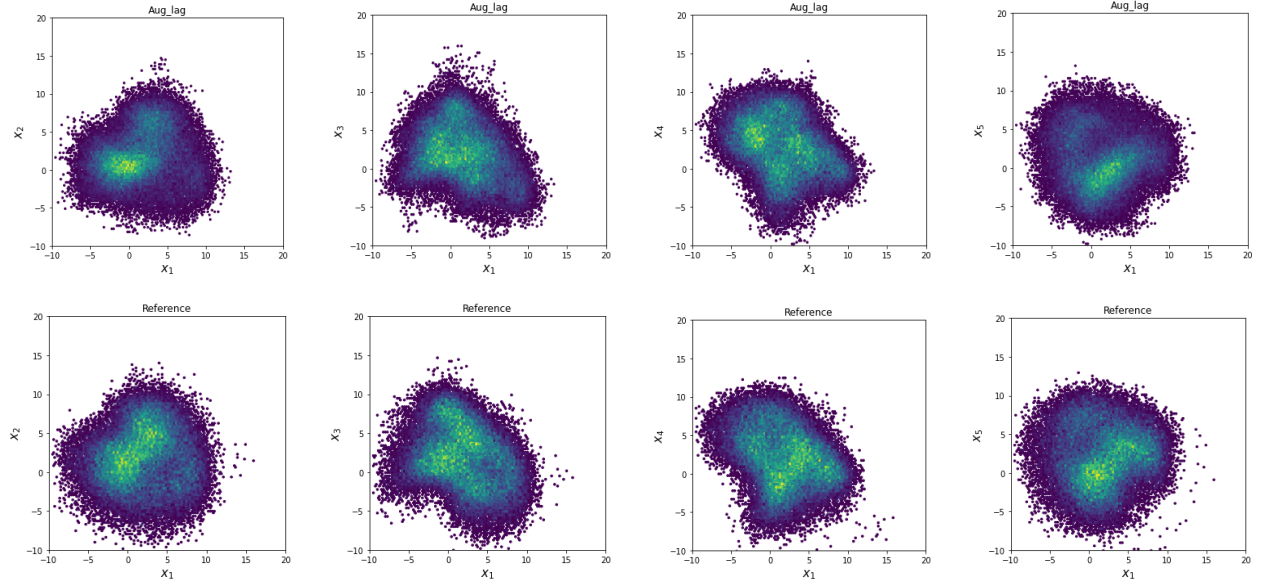


Figure 4.5: Lorenz-96 system (4.5) with  $N = 5$ ,  $F = 8$ , and  $D = 0.05$ . **Top:** invariant density projections from the PINN-IMSM reconstruction. **Bottom:** corresponding reference invariant density from the true system. Two-dimensional projection histograms onto  $(x_1, x_2)$ ,  $(x_1, x_3)$ ,  $(x_1, x_4)$ , and  $(x_1, x_5)$  planes.

## 5 Conclusion

In this paper, we introduced PINN-IMSM, a novel mesh-free framework for reconstructing dynamical systems from unlabeled point-cloud observational data that capture the asymptotic statistical behavior of the underlying system without explicit temporal information. By adopting an Eulerian perspective and reformulating the stationary FP equation in terms of the score function, our approach overcomes the reliance on time-labeled trajectories required by Lagrangian approaches. The core innovation of the proposed PINN-IMSM method is the integration of denoising score matching with physics-informed neural networks: the score function of the invariant measure is estimated directly from data, circumventing costly density estimation, and is then embedded into a PINN to reconstruct the velocity field under the PDE constraint. To ensure well-posedness in high-dimensional settings, the reconstruction is reformulated as a PDE-constrained optimization that seeks the velocity field with minimal  $L^2$ -norm, solved efficiently using the stochastic augmented Lagrangian method. Numerical experiments on benchmark problems demonstrate that

PINN-IMSM achieves accurate and stable reconstruction of dynamical systems, successfully handling problems up to five dimensions. This represents a significant advancement over existing mesh-based Eulerian approaches, which are typically limited to low-dimensional problems ( $d \leq 3$ ) due to the curse of dimensionality. Moreover, the method shows robustness in scenarios with incomplete velocity information, faithfully recovering chaotic attractors and complex dynamical behaviors from sparse observational data. The theoretical foundation of our approach is strengthened by our proof that, under suitable conditions, the inverse problem admits a unique solution that depends continuously on the score function.

Future work will extend the current framework to systems with non-constant or anisotropic diffusion coefficients and develop theoretical tools for more general classes of stochastic dynamical systems. Further promising directions include incorporating uncertainty quantification and exploring applications to high-dimensional problems in molecular dynamics, climate modeling, and biological systems.

## Acknowledgments

Research work of Y. Chen and X. Zhong was partially supported by National Key R&D Program of China 2024YFA1012302 and NSFC Grant 11871428.

## References

- [1] Ricky TQ Chen, Yulia Rubanova, Jesse Bettencourt, and David K Duvenaud. Neural ordinary differential equations. *Advances in neural information processing systems*, 31, 2018.
- [2] Gavin D Portwood, Peetak P Mitra, Mateus Dias Ribeiro, Tan Minh Nguyen, Balasubramanya T Nadiga, Juan A Saenz, Michael Chertkov, Animesh Garg, Anima Anandkumar, Andreas Dengel, et al. Turbulence forecasting via neural ode. *arXiv preprint arXiv:1911.05180*, 2019.
- [3] Alec J Linot and Michael D Graham. Data-driven reduced-order modeling of spatiotemporal chaos with neural ordinary differential equations. *Chaos: An Interdisciplinary Journal of Nonlinear Science*, 32(7), 2022.
- [4] Alec J Linot, Joshua W Burby, Qi Tang, Prasanna Balaprakash, Michael D Graham, and Romit Maulik. Stabilized neural ordinary differential equations for long-time forecasting of dynamical systems. *Journal of Computational Physics*, 474:111838, 2023.
- [5] Steven L Brunton, Joshua L Proctor, and J Nathan Kutz. Discovering governing equations from data by sparse identification of nonlinear dynamical systems. *Proceedings of the national academy of sciences*, 113(15):3932–3937, 2016.
- [6] Daniel A Messenger and David M Bortz. Weak sindy: Galerkin-based data-driven model selection. *Multiscale Modeling & Simulation*, 19(3):1474–1497, 2021.

- [7] Urban Fasel, J Nathan Kutz, Bingni W Brunton, and Steven L Brunton. Ensemble-sindy: Robust sparse model discovery in the low-data, high-noise limit, with active learning and control. *Proceedings of the Royal Society A*, 478(2260):20210904, 2022.
- [8] Zhijun Zeng, Pipi Hu, Chenglong Bao, Yi Zhu, and Zuoqiang Shi. Reconstruction of dynamical systems from data without time labels. *arXiv preprint arXiv:2312.04038*, 2023.
- [9] Yunan Yang, Levon Nurbekyan, Elisa Negrini, Robert Martin, and Mirjeta Pasha. Optimal transport for parameter identification of chaotic dynamics via invariant measures. *SIAM Journal on Applied Dynamical Systems*, 22(1):269–310, 2023.
- [10] Jonah Botvinick-Greenhouse, Robert Martin, and Yunan Yang. Learning dynamics on invariant measures using pde-constrained optimization. *Chaos: An Interdisciplinary Journal of Nonlinear Science*, 33(6), 2023.
- [11] Maziar Raissi, Paris Perdikaris, and George E Karniadakis. Physics-informed neural networks: A deep learning framework for solving forward and inverse problems involving nonlinear partial differential equations. *Journal of Computational physics*, 378:686–707, 2019.
- [12] George Em Karniadakis, Ioannis G Kevrekidis, Lu Lu, Paris Perdikaris, Sifan Wang, and Liu Yang. Physics-informed machine learning. *Nature Reviews Physics*, 3(6):422–440, 2021.
- [13] Sifan Wang, Xinling Yu, and Paris Perdikaris. When and why pinns fail to train: a neural tangent kernel perspective. *Journal of Computational Physics*, 449:110768, 2022.
- [14] Ameya D Jagtap, Ehsan Kharazmi, and George Em Karniadakis. Conservative physics-informed neural networks on discrete domains for conservation laws: applications to forward and inverse problems. *Computer Methods in Applied Mechanics and Engineering*, 365:113028, 2020.
- [15] Simon Stock, Jochen Stiasny, Davood Babazadeh, Christian Becker, and Spyros Chatzivasileiadis. Bayesian physics-informed neural networks for robust system identification of power systems. In *2023 IEEE Belgrade PowerTech*, pages 1–6. IEEE, 2023.
- [16] Lu Lu, Pengzhan Jin, Guofei Pang, Zhongqiang Zhang, and George Em Karniadakis. Learning nonlinear operators via deeponet based on the universal approximation theorem of operators. *Nature machine intelligence*, 3(3):218–229, 2021.
- [17] Zongyi Li, Nikola Borislavov Kovachki, Kamyar Azizzadenesheli, Burigede liu, Kaushik Bhattacharya, Andrew Stuart, and Anima Anandkumar. Fourier neural operator for parametric partial differential equations. In *International Conference on Learning Representations*, 2021.
- [18] Anima Anandkumar, Kamyar Azizzadenesheli, Kaushik Bhattacharya, Nikola Kovachki, Zongyi Li, Burigede Liu, and Andrew Stuart. Neural operator: graph kernel network for partial differential equations. In *ICLR 2020 workshop on integration of deep neural models and differential equations*, 2020.

[19] Maarten V. de Hoop, Daniel Zhengyu Huang, Elizabeth Qian, and Andrew M. Stuart. The cost-accuracy trade-off in operator learning with neural networks. *Journal of Machine Learning*, 1(3), 2022.

[20] Derick Nganyu Tanyu, Jianfeng Ning, Tom Freudenberg, Nick Heilenkötter, Andreas Rademacher, Uwe Iben, and Peter Maass. Deep learning methods for partial differential equations and related parameter identification problems. *Inverse Problems*, 39(10):103001, 2023.

[21] Zongyi Li, Hongkai Zheng, Nikola Kovachki, David Jin, Haoxuan Chen, Burigede Liu, Kam-yar Azizzadenesheli, and Anima Anandkumar. Physics-informed neural operator for learning partial differential equations. *ACM/JMS Journal of Data Science*, 1(3):1–27, 2024.

[22] Shawn G Rosofsky, Hani Al Majed, and EA Huerta. Applications of physics informed neural operators. *Machine Learning: Science and Technology*, 4(2):025022, 2023.

[23] Aapo Hyvärinen and Peter Dayan. Estimation of non-normalized statistical models by score matching. *Journal of Machine Learning Research*, 6(4), 2005.

[24] Yang Song, Sahaj Garg, Jiaxin Shi, and Stefano Ermon. Sliced score matching: a scalable approach to density and score estimation. In *Uncertainty in Artificial Intelligence*, pages 574–584. PMLR, 2020.

[25] Alp Dener, Marco Andres Miller, Randy Michael Churchill, Todd Munson, and Choong-Seock Chang. Training neural networks under physical constraints using a stochastic augmented lagrangian approach. *arXiv preprint arXiv:2009.07330*, 2020.

[26] Wen Huang, Min Ji, Zhenxin Liu, and Yingfei Yi. Steady states of fokker–planck equations: I. existence. *Journal of Dynamics and Differential Equations*, 27:721–742, 2015.

[27] Igor V Ovchinnikov. Introduction to supersymmetric theory of stochastics. *Entropy*, 18(4):108, 2016.

[28] Peter H Baxendale and Sergey V Lototsky. *Stochastic differential equations: theory and applications*, volume 2. World Scientific, 2007.

[29] Gerhard Keller. Stochastic stability in some chaotic dynamical systems. *Monatshefte für Mathematik*, 94(4):313–333, 1982.

[30] Lai-Sang Young. Stochastic stability of hyperbolic attractors. *Ergodic Theory and Dynamical Systems*, 6(2):311–319, 1986.

[31] William Cowieson and Lai-Sang Young. Srb measures as zero-noise limits. *Ergodic Theory and dynamical systems*, 25(4):1115–1138, 2005.

[32] Richard Ernest Bellman. *Adaptive control processes: a guided tour*. Princeton University Press, Princeton, NJ, 1961.

- [33] Jiaming Song, Chenlin Meng, and Stefano Ermon. Score-based generative modeling through stochastic differential equations. In *International Conference on Learning Representations*, 2021.
- [34] Jonathan Ho, Ajay Jain, and Pieter Abbeel. Denoising diffusion probabilistic models. In *Advances in Neural Information Processing Systems*, volume 33, pages 6840–6851, 2020.
- [35] Pascal Vincent. A connection between score matching and denoising autoencoders. *Neural computation*, 23(7):1661–1674, 2011.
- [36] Yang Song and Stefano Ermon. Generative modeling by estimating gradients of the data distribution. *Advances in neural information processing systems*, 32, 2019.
- [37] Yang Song and Stefano Ermon. Improved techniques for training score-based generative models. *Advances in neural information processing systems*, 33:12438–12448, 2020.
- [38] Alfio Quarteroni and Alberto Valli. *Numerical approximation of partial differential equations*, volume 23. Springer Science & Business Media, 2008.
- [39] Susanne C Brenner. *The mathematical theory of finite element methods*. Springer, 2008.
- [40] Atilim Gunes Baydin, Barak A Pearlmutter, Alexey Andreyevich Radul, and Jeffrey Mark Siskind. Automatic differentiation in machine learning: a survey. *Journal of Machine Learning Research*, 18(153):1–43, 2017.
- [41] Diederik P Kingma and Jimmy Ba. Adam: a method for stochastic optimization. *arXiv preprint arXiv:1412.6980*, 2014.
- [42] Dong C Liu and Jorge Nocedal. On the limited memory bfgs method for large scale optimization. *Mathematical Programming*, 45(1-3):503–528, 1989.
- [43] Teeratorn Kadeethum, Thomas M Jørgensen, and Hamidreza M Nick. Physics-informed neural networks for solving inverse problems of nonlinear biot’s equations: batch training. In *ARMA US Rock Mechanics/Geomechanics Symposium*, pages ARMA–2020. ARMA, 2020.
- [44] Ivan Depina, Saket Jain, Sigurdur Mar Valsson, and Hrvoje Gotovac. Application of physics-informed neural networks to inverse problems in unsaturated groundwater flow. *Georisk: Assessment and Management of Risk for Engineered Systems and Geohazards*, 16(1):21–36, 2022.
- [45] Quan Guo, Yue Zhao, Chunhui Lu, and Jian Luo. High-dimensional inverse modeling of hydraulic tomography by physics informed neural network (ht-pinn). *Journal of Hydrology*, 616:128828, 2023.
- [46] Steffen Eger, Paul Youssef, and Iryna Gurevych. Is it time to swish? comparing deep learning activation functions across nlp tasks. In *Proceedings of the 2018 Conference on Empirical Methods in Natural Language Processing*, pages 4415–4424, 2018.

[47] Maziar Raissi, Alireza Yazdani, and George Em Karniadakis. Hidden fluid mechanics: Learning velocity and pressure fields from flow visualizations. *Science*, 367(6481):1026–1030, 2020.

[48] Ian Goodfellow. Deep learning, 2016.

[49] Kurt Hornik, Maxwell Stinchcombe, and Halbert White. Multilayer feedforward networks are universal approximators. *Neural networks*, 2(5):359–366, 1989.

[50] Tianping Chen and Hong Chen. Universal approximation to nonlinear operators by neural networks with arbitrary activation functions and its application to dynamical systems. *IEEE transactions on neural networks*, 6(4):911–917, 1995.

[51] Lu Lu, Raphaël Pestourie, Wenjie Yao, Zhicheng Wang, Francesc Verdugo, and Steven G. Johnson. Physics-informed neural networks with hard constraints for inverse design. *SIAM Journal on Scientific Computing*, 43(6):B1105–B1132, 2021.

[52] Yaohua Zang, Gang Bao, Xiaojing Ye, and Haomin Zhou. Weak adversarial networks for high-dimensional partial differential equations. *Journal of Computational Physics*, 411:109409, 2020.

[53] Magnus R Hestenes. Multiplier and gradient methods. *Journal of optimization theory and applications*, 4(5):303–320, 1969.

[54] Michael JD Powell. A method for nonlinear constraints in minimization problems. *Optimization*, pages 283–298, 1969.

[55] Ilya Loshchilov and Frank Hutter. Decoupled weight decay regularization. In *International Conference on Learning Representations*, 2018.

[56] John Guckenheimer. Dynamics of the van der pol equation. *IEEE Transactions on Circuits and Systems*, 27(11):983–989, 2003.

[57] Julien Tailleur and Michael E Cates. Statistical mechanics of interacting run-and-tumble bacteria. *Physical review letters*, 100(21):218103, 2008.

[58] Stefano Luzzatto, Ian Melbourne, and Frederic Paccaut. The lorenz attractor is mixing. *Communications in Mathematical Physics*, 260:393–401, 2005.

[59] Edward Ott, Brian R Hunt, Istvan Szunyogh, Aleksey V Zimin, Eric J Kostelich, Matteo Corazza, Eugenia Kalnay, DJ Patil, and James A Yorke. A local ensemble kalman filter for atmospheric data assimilation. *Tellus A: Dynamic Meteorology and Oceanography*, 56(5):415–428, 2004.

[60] Alireza Karimi and Mark R Paul. Extensive chaos in the lorenz-96 model. *Chaos: An interdisciplinary journal of nonlinear science*, 20(4), 2010.

[61] Steven George Krantz and Harold R Parks. *The implicit function theorem: history, theory, and applications*. Springer Science & Business Media, 2002.

- [62] Alexandre Ern, Jean-Luc Guermond, et al. *Finite elements II*. Springer, 2021.
- [63] Lawrence C Evans. *Partial differential equations*, volume 19. American Mathematical Society, 2022.
- [64] David Gilbarg, Neil S Trudinger, David Gilbarg, and NS Trudinger. *Elliptic partial differential equations of second order*, volume 224. Springer, 1977.

## A Proof of Theorem 3.1

In this section, we show the detailed proof of Theorem 3.1 in Section 3.3.2. This section is organized as follows: in Section A.1, we introduce the necessary notations, function spaces, norms, and preliminary lemmas. In Section A.2, we present the existence and regularity of the forward problem, which establishes an important relationship between the score function and the velocity field. Finally, in Section A.3, we complete the proof of Theorem 3.1 that ensuring the well-posedness of the inverse problem.

### A.1 Preliminaries

We first introduce function spaces used throughout the proof. We consider the standard continuous function space  $C^m(\Omega)$  for  $m \geq 2$  equipped with the norm  $\|\cdot\|_{C^m}$ , and the space  $C^{m,1}(\Omega)$  of  $m$ -times continuously differentiable functions whose  $m$ -th derivatives are Lipschitz continuous. We also employ the Sobolev spaces  $W^{m,p}(\Omega)$  for  $m \geq 0$  and  $1 \leq p \leq \infty$  equipped with the norm  $\|\cdot\|_{W^{m,p}}$ . The Hilbert space is denoted by  $H^m(\Omega)$  for  $m \geq 0$  equipped with the norm  $\|\cdot\|_{H^m}$ ; in particular,  $H^0(\Omega) = L^2(\Omega)$  with the  $L^2$  norm denoted simply by  $\|\cdot\|$ . The dual space of  $H^1(\Omega)$  is denoted by  $H^{-1}(\Omega)$ . For vector fields we use the standard Hilbert space

$$H(\text{div}; \Omega) := \left\{ \mathbf{v} \in L^2(\Omega; \mathbb{R}^d) : \nabla \cdot \mathbf{v} \in L^2(\Omega) \right\}, \quad \|\mathbf{v}\|_{H(\text{div})}^2 := \|\mathbf{v}\|_{L^2}^2 + \|\nabla \cdot \mathbf{v}\|_{L^2}^2.$$

We also employ the following subspaces and local spaces:

$$H_{\circ}^1(\Omega) := \left\{ w \in H^1(\Omega) : \int_{\Omega} w \, dx = 0 \right\}.$$

and  $H_{\text{loc}}^m(\Omega)$  consisting of functions belonging to  $H^m$  on every compact subset of  $\Omega$ .

The following classical results are essential for our analysis.

**Theorem A.1** (Implicit Function Theorem [61, Theorem 3.3.1]). Let  $X, Y, Z$  be Banach spaces and let  $U \subset X, V \subset Y$  be open sets. Suppose  $F : U \times V \rightarrow Z$  is continuously Fréchet differentiable. If there exist  $(x_0, y_0) \in U \times V$  such that

$$F(x_0, y_0) = 0 \quad \text{and} \quad D_y F(x_0, y_0) : Y \rightarrow Z \text{ is a bounded linear isomorphism,}$$

then there exist neighborhoods  $U_0 \subset U$  of  $x_0$  and  $V_0 \subset V$  of  $y_0$ , and a unique continuously differentiable mapping  $g : U_0 \rightarrow V_0$  such that

$$F(x, g(x)) = 0 \quad \text{for all } x \in U_0, \quad g(x_0) = y_0.$$

Moreover, if  $F \in C^k$  then  $g \in C^k$ , and  $Dg(x) = -(D_y F(x, g(x)))^{-1} D_x F(x, g(x))$  for  $x \in U_0$ .

## A.2 Existence and regularity of the forward problem

We consider the stationary FP equation (2.8) with the boundary condition (2.7) in divergence form

$$\nabla \cdot (-D\nabla \rho + \rho \mathbf{v}) = 0 \quad \text{in } \Omega, \quad (\text{A.1})$$

$$(D\nabla \rho - \rho \mathbf{v}) \cdot \mathbf{n} = 0 \quad \text{on } \partial\Omega, \quad (\text{A.2})$$

where  $\mathbf{v}$  is a given velocity.

The weak formulation of the problem (A.1) is: find  $\rho \in H^1(\Omega)$  such that

$$a(\rho, \varphi) := \int_{\Omega} (D\nabla \rho - \rho \mathbf{v}) \cdot \nabla \varphi \, dx = 0, \quad \forall \varphi \in H^1(\Omega). \quad (\text{A.3})$$

The bilinear form  $a(\cdot, \cdot)$  is bounded on  $H^1(\Omega) \times H^1(\Omega)$ , since by Cauchy-Schwarz inequality, for any  $u, \varphi \in H^1(\Omega)$ ,

$$|a(u, \varphi)| \leq D \|\nabla u\|_{L^2} \|\nabla \varphi\|_{L^2} + \|\mathbf{v}\|_{L^\infty} \|u\|_{L^2} \|\nabla \varphi\|_{L^2} \leq C \|u\|_{H^1} \|\varphi\|_{H^1}. \quad (\text{A.4})$$

Moreover, a direct computation yields the Gårding inequality.

$$a(u, u) = D \|\nabla u\|_{L^2}^2 - \int_{\Omega} u \mathbf{v} \cdot \nabla u \, dx \geq \frac{D}{2} \|\nabla u\|_{L^2}^2 - \frac{\|\mathbf{v}\|_{L^\infty}^2}{2D} \|u\|_{L^2}^2. \quad (\text{A.5})$$

The following proposition clarifies that a weak solution satisfies the boundary condition. Its proof follows the arguments of [62, Proposition 31.13] with the diffusion flux taken as  $\sigma = -D\nabla \rho + \rho \mathbf{v}$ .

**Proposition 1** (Weak solution). Let  $\rho$  solve (A.3) with  $\mathbf{v} \in L^\infty(\Omega; \mathbb{R}^d)$ . Then, the PDE in (A.1) holds almost everywhere in  $\Omega$  and the boundary condition holds almost everywhere on  $\partial\Omega$ .

**Lemma A.1** (Existence, uniqueness and interior regularity). Assume  $\mathbf{v} \in L^\infty(\Omega; \mathbb{R}^d)$  and  $\nabla \cdot \mathbf{v} \in L^\infty(\Omega)$ . Let  $C_P$  be the Poincaré constant on  $H_0^1(\Omega)$ , i.e.,  $\|w\|_{L^2} \leq C_P \|\nabla w\|_{L^2}$  for all  $w \in H_0^1(\Omega)$ . If the diffusion coefficient satisfies  $D > \|\mathbf{v}\|_{L^\infty(\Omega)} C_P$ , then the boundary value problem (A.1) admits a unique weak solution  $\rho \in H^1(\Omega)$  satisfying the normalization  $\int_{\Omega} \rho \, dx = 1$ . Moreover,  $\rho \in W_{\text{loc}}^{2,p}(\Omega)$  for all  $1 < p < \infty$ . If, in addition,  $\mathbf{v} \in W^{m,\infty}(\Omega)$  for some integer  $m \geq 2$ , then  $\rho \in H_{\text{loc}}^m(\Omega)$ .

*Proof.* The function  $\rho \in H^1(\Omega)$  with the normalization condition  $\int_{\Omega} \rho \, dx = 1$  can be decomposed as

$$\rho = c + u,$$

where the constant  $c = \frac{1}{|\Omega|}$ , and  $u \in H_0^1(\Omega)$ . Then the problem (A.3) is equivalent to: find  $u \in H_0^1(\Omega)$  such that

$$a(u, \varphi) = \int_{\Omega} c \mathbf{v} \cdot \nabla \varphi \, dx \triangleq F(\varphi), \quad \forall \varphi \in H_0^1(\Omega). \quad (\text{A.6})$$

Clearly  $F$  is a bounded linear functional on  $H_0^1(\Omega)$ . Indeed, for any  $\varphi \in H_0^1(\Omega)$ ,

$$|F(\varphi)| = \left| \int_{\Omega} c \mathbf{v} \cdot \nabla \varphi \, dx \right| \leq c \|\mathbf{v}\|_{L^\infty(\Omega)} \|\nabla \varphi\|_{L^2(\Omega)} \leq C \|\varphi\|_{H^1(\Omega)}.$$

Moreover, for any  $w \in H_\diamond^1(\Omega)$ , it follows from the Gårding inequality (A.5) and the Poincaré inequality that

$$a(w, w) \geq \frac{D}{2} \|\nabla w\|_{L^2}^2 - \frac{\|\mathbf{v}\|_{L^\infty}^2}{2D} \|w\|_{L^2}^2 \geq \left( \frac{D}{2} - \frac{\|\mathbf{v}\|_{L^\infty}^2}{2D} C_P^2 \right) \|\nabla w\|_{L^2}^2 = \kappa \|\nabla w\|_{L^2}^2,$$

where  $\kappa = \frac{D}{2} - \frac{\|\mathbf{v}\|_{L^\infty}^2}{2D} C_P^2$ . The condition  $D > \|\mathbf{v}\|_{L^\infty(\Omega)} C_P$  ensures  $\kappa > 0$ . Since  $\|w\|_{H^1}^2 = \|w\|_{L^2}^2 + \|\nabla w\|_{L^2}^2 \leq (1 + C_P^2) \|\nabla w\|_{L^2}^2$  on  $H_\diamond^1(\Omega)$ , we obtain

$$a(w, w) \geq \frac{\kappa}{1 + C_P^2} \|w\|_{H^1}^2.$$

Thus the bilinear form  $a(\cdot, \cdot)$  is coercive on  $H_\diamond^1(\Omega)$ . Together with its boundedness established in (A.4), the Lax-Milgram theorem [63, Theorem 6.2]) yields a unique  $u \in H_\diamond^1(\Omega)$  solving (A.6), which also solves (A.3). Setting  $\rho = c + u$  gives a weak solution of (A.1) with  $\int_\Omega \rho \, dx = 1$ .

It follows from Proposition 1 that  $\rho$  satisfies (A.1) almost everywhere, which can be rewritten as the non-divergence form:

$$-D\Delta\rho + \mathbf{v} \cdot \nabla\rho + (\nabla \cdot \mathbf{v})\rho = 0.$$

Standard  $L^p$ -regularity [64, Theorems 9.11 and 9.15] implies that  $\rho$  belongs to  $W_{\text{loc}}^{2,p}(\Omega)$  for all  $1 < p < \infty$ . Furthermore, if  $\mathbf{v} \in W^{m,\infty}$  for some integer  $m \geq 2$ , then  $\nabla \cdot \mathbf{v} \in W^{m-1,\infty}$ . Since  $W^{k,\infty}(\Omega) \hookrightarrow C^{k-1,1}(\overline{\Omega})$  for  $k \geq 1$  by the Sobolev embedding theorem, the coefficients of the elliptic equation are of class  $C^{m-2,1}$  in the interior. Applying higher-order interior regularity theory for elliptic equations [64, Theorem 8.12]), we obtain  $\rho \in H_{\text{loc}}^m(\Omega)$ .  $\square$

The condition  $D > \|\mathbf{v}\|_{L^\infty(\Omega)} C_P$  serves as a sufficient condition to ensure the coercivity of the bilinear form  $a(\cdot, \cdot)$ , thereby enabling the direct application of the Lax-Milgram theorem. Physically, this corresponds to a diffusion-dominated regime (or a small Péclet number regime), where the stochastic diffusion is strong enough to counteract the deterministic drift, ensuring a stable stationary distribution. While the well-posedness of the FP equation may hold under weaker assumptions (e.g., via the Fredholm alternative for convection-dominated flows), this condition provides a rigorous and simplified framework sufficient for establishing the stability of the inverse problem.

The normalization condition  $\int_\Omega \rho \, dx = 1$  is consistent with the constraints (2.3) for the FP equation. Lemma A.1 guarantees the existence and interior regularity of the stationary density  $\rho$ . Consequently, whenever  $\rho > 0$  on a subset  $\Omega' \subset \Omega$  with  $\overline{\Omega'}$  compact in  $\Omega$ , and  $\rho \in H_{\text{loc}}^m(\Omega)$  with  $m > d/2 + 1$ , its score function

$$\mathbf{s} = \nabla \log \rho = \frac{\nabla \rho}{\rho}$$

is well defined on  $\Omega'$  and belongs to  $H^{m-1}(\Omega')$ . In what follows we simply take  $\mathbf{s}$  as a given element of  $W^{1,\infty}(\Omega; \mathbb{R}^d)$  and study the constrained optimization problem associated with  $\mathbf{s}$ . This regularity assumption is natural in the context of elliptic regularity theory: for sufficiently smooth velocity fields  $\mathbf{v}$  and under a uniform positivity condition on  $\rho$ , the stationary FP equation indeed yields a score function with bounded first derivatives.

### A.3 Well-posedness of the constrained optimization

We now analyze the optimization problem (3.5)

$$\min_{\mathbf{v}} J(\mathbf{v}) := \frac{1}{2} \|\mathbf{v}\|_{L^2(\Omega)}^2 \quad \text{subject to} \quad \tilde{\mathcal{N}}(\mathbf{s}, \mathbf{v}) = 0 \quad \text{in } L^2(\Omega). \quad (\text{A.7})$$

where  $\tilde{\mathcal{N}}(\mathbf{s}, \mathbf{v}) = \mathbf{s} \cdot \mathbf{v} + \nabla \cdot \mathbf{v} - D(|\mathbf{s}|^2 + \nabla \cdot \mathbf{s})$ . Throughout this subsection, we assume the score  $\mathbf{s}$  is given with the regularity that can be justified under suitable conditions on the velocity field, as discussed after Lemma A.1.

**Lemma A.2** (Existence and uniqueness of the minimizer). Let  $\mathbf{s} \in L^\infty(\Omega; \mathbb{R}^d)$  with  $\nabla \cdot \mathbf{s} \in L^2(\Omega)$ . Define the linear operator  $C_s : H(\text{div}; \Omega) \rightarrow L^2(\Omega)$ :

$$C_s(\mathbf{v}) = \mathbf{s} \cdot \mathbf{v} + \nabla \cdot \mathbf{v},$$

and let  $g_s = D(|\mathbf{s}|^2 + \nabla \cdot \mathbf{s})$ . Then the feasible set

$$\mathcal{V}_{\text{ad}}(\mathbf{s}) := \{\mathbf{v} \in H(\text{div}; \Omega) : C_s(\mathbf{v}) = g_s\}$$

is a nonempty closed affine subspace of  $H(\text{div}; \Omega)$ . Consequently, the problem (A.7) admits a unique minimizer  $\mathbf{v}^* \in \mathcal{V}_{\text{ad}}(\mathbf{s})$ .

*Proof.* The set  $\mathcal{V}_{\text{ad}}(\mathbf{s})$  is affine because it is the inverse image of a single element under the linear operator  $C_s$ . It is nonempty since  $\mathbf{v}_0 = D\mathbf{s} \in H(\text{div}; \Omega)$  satisfies

$$C_s(\mathbf{v}_0) = \mathbf{s} \cdot (D\mathbf{s}) + \nabla \cdot (D\mathbf{s}) = D(|\mathbf{s}|^2 + \nabla \cdot \mathbf{s}) = g_s.$$

For any  $\mathbf{v} \in H(\text{div}; \Omega)$ ,

$$\|C_s(\mathbf{v})\|_{L^2} \leq \|\mathbf{s}\|_{L^\infty} \|\mathbf{v}\|_{L^2} + \|\nabla \cdot \mathbf{v}\|_{L^2} \leq C \|\mathbf{v}\|_{H(\text{div})},$$

hence  $C_s$  is continuous and  $\mathcal{V}_{\text{ad}}(\mathbf{s})$  is closed.

The objective  $J(\mathbf{v}) = \frac{1}{2} \|\mathbf{v}\|_{L^2(\Omega)}^2$  is strongly continuous and strictly convex on the Hilbert space  $H(\text{div}; \Omega)$ . Thus it is also weakly lower semicontinuous. The constraint in (A.7) can be written as  $C_s(\mathbf{v}) = g_s$  in  $L^2(\Omega)$  (via the continuous embedding  $H(\text{div}; \Omega) \hookrightarrow L^2(\Omega; \mathbb{R}^d)$ ). Let  $\{\mathbf{v}_n\} \subset \mathcal{V}_{\text{ad}}(\mathbf{s})$  be a minimizing sequence. Since  $\{J(\mathbf{v}_n)\}$  is bounded,  $\{\mathbf{v}_n\}$  is bounded in  $L^2(\Omega)$ ; hence, up to a subsequence,  $\mathbf{v}_n \rightharpoonup \mathbf{v}^*$  weakly in  $L^2(\Omega)$ . Because  $\mathcal{V}_{\text{ad}}(\mathbf{s})$  is a closed convex subset of  $H(\text{div}; \Omega)$  and  $C_s$  is continuous, the limit  $\mathbf{v}^*$  is feasible, i.e.,  $\mathbf{v}^* \in \mathcal{V}_{\text{ad}}(\mathbf{s})$ . By weak lower semicontinuity of  $J$ ,

$$J(\mathbf{v}^*) \leq \liminf_{n \rightarrow \infty} J(\mathbf{v}_n) = \inf_{\mathbf{v} \in \mathcal{V}_{\text{ad}}(\mathbf{s})} J(\mathbf{v}),$$

so  $\mathbf{v}^*$  is a minimizer. Uniqueness follows from strict convexity of  $J$  on the convex set  $\mathcal{V}_{\text{ad}}(\mathbf{s})$ .  $\square$

Having established the existence and uniqueness of the minimizer for problem (A.7), we next analyze the stability of the solution operator  $\mathbf{s} \mapsto \mathbf{v}^*$  with respect to perturbations in the score function.

**Lemma A.3** (Continuity of the solution map  $s \mapsto \mathbf{v}^*$ ). Assume  $s \in W^{1,\infty}(\Omega; \mathbb{R}^d)$  with  $q_s \geq 0$  almost everywhere in  $\Omega$ , where

$$q_s = |s|^2 + \nabla \cdot s. \quad (\text{A.8})$$

Let  $\mathbf{v}^* \in H(\text{div}; \Omega)$  be the unique minimizer of (A.7). Then there exists a neighborhood  $U \subset W^{1,\infty}(\Omega; \mathbb{R}^d)$  of  $s$  such that, for every  $\tilde{s} \in U$ , if  $\tilde{\mathbf{v}}^*$  denotes the unique optimizer associated with  $\tilde{s}$ , then

$$\|\mathbf{v}^* - \tilde{\mathbf{v}}^*\|_{L^2(\Omega)} \leq C \|s - \tilde{s}\|_{W^{1,\infty}(\Omega)},$$

where the constant  $C > 0$  depends monotonically on  $D$ ,  $\Omega$ , and  $s$ .

*Proof.* We first characterize the minimizer of the constrained optimization problem (A.7) via the Lagrange multiplier method by introducing the Lagrangian functional on  $H(\text{div}; \Omega) \times H_\diamond^1(\Omega)$ :

$$\mathcal{L}(\mathbf{v}, \lambda; s) = \frac{1}{2} \|\mathbf{v}\|_{L^2}^2 + (s \cdot \mathbf{v} + \nabla \cdot \mathbf{v} - Dq_s, \lambda)_{L^2},$$

where  $(\cdot, \cdot)_{L^2}$  denotes the  $L^2$ -inner product, i.e.,  $(f, g)_{L^2} := \int_\Omega f(x)g(x) dx$ . Since  $\mathbf{v}^*$  is a minimizer of (A.7), the first-order optimality condition implies that the Gâteaux derivative of  $\mathcal{L}$  with respect to  $\mathbf{v}$  vanishes at  $\mathbf{v}^*$  in every direction  $\phi \in H(\text{div}; \Omega)$ , i.e.,

$$\delta_\mathbf{v} \mathcal{L}(\mathbf{v}^*, \lambda)[\phi] = (\mathbf{v}^*, \phi)_{L^2} + (s \cdot \phi + \nabla \cdot \phi, \lambda)_{L^2} = 0. \quad (\text{A.9})$$

Recall that the FP equation (2.8) is accompanied by the no-flux boundary condition (2.7),  $(D\nabla \rho - \rho \mathbf{v}) \cdot \mathbf{n} = 0$ , which in terms of the score  $s = \nabla \log \rho = \nabla \rho / \rho$  reads  $(\mathbf{v} - Ds) \cdot \mathbf{n} = 0$ . We therefore require that the recovered velocity field satisfy the same condition. Consequently, the admissible directions  $\phi$  should preserve this boundary condition, i.e.,  $\phi \cdot \mathbf{n} = 0$  on  $\partial\Omega$ .

For  $\lambda \in H_\diamond^1(\Omega)$  and  $\phi \in H(\text{div}; \Omega)$ , we interpret the term  $(\lambda, \nabla \cdot \phi)_{L^2}$  in (A.9) in the distributional sense:

$$(\lambda, \nabla \cdot \phi)_{L^2} = -(\nabla \lambda, \phi)_{L^2} + \int_{\partial\Omega} \lambda \phi \cdot \mathbf{n} dx = -(\nabla \lambda, \phi)_{L^2}, \quad (\text{A.10})$$

where the boundary integral vanishes due to  $\phi \cdot \mathbf{n} = 0$ . Substituting this into (A.9) yields

$$(\mathbf{v}^*, \phi)_{L^2} - (\nabla \lambda - \lambda s, \phi)_{L^2} = 0 \quad \forall \phi \in H(\text{div}; \Omega),$$

from which we infer the pointwise identity

$$\mathbf{v}^* = \nabla \lambda - \lambda s. \quad (\text{A.11})$$

Substituting  $\mathbf{v}^* = \nabla \lambda - \lambda s$  into the constraint  $s \cdot \mathbf{v}^* + \nabla \cdot \mathbf{v}^* = D(|s|^2 + \nabla \cdot s)$  gives

$$-\Delta \lambda + q_s \lambda = -Dq_s \quad \text{in } \Omega.$$

We supplement this equation with the homogeneous Neumann condition  $\partial_n \lambda = 0$  on  $\partial\Omega$  and the normalization  $\int_\Omega \lambda dx = 0$  to obtain a well-posed problem. Its weak formulation reads: find  $\lambda \in H_\diamond^1(\Omega)$  such that

$$a_s(\lambda, \varphi) = \int_\Omega -Dq_s \varphi dx, \quad \forall \varphi \in H_\diamond^1(\Omega), \quad (\text{A.12})$$

where  $a_s$  is the bilinear form defined as

$$a_s(\lambda, \varphi) = \int_{\Omega} \nabla \lambda \cdot \nabla \varphi + q_s \lambda \varphi \, dx, \quad \lambda, \varphi \in H_{\diamond}^1(\Omega). \quad (\text{A.13})$$

If  $q_s \geq 0$ , then the bilinear form  $a_s$  is coercive and bounded on  $H_{\diamond}^1(\Omega) \times H_{\diamond}^1(\Omega)$ . In fact, by Cauchy-Schwarz inequality, for  $\lambda, \varphi \in H_{\diamond}^1(\Omega)$ , we have

$$|a_s(\lambda, \varphi)| \leq \|\nabla \lambda\|_{L^2} \|\nabla \varphi\|_{L^2} + |q_s| L^{\infty} \|\lambda\|_{L^2} \|\varphi\|_{L^2} \leq C \|\lambda\|_{H^1} \|\varphi\|_{H^1}, \quad (\text{A.14})$$

$$|a_s(\lambda, \lambda)| = \|\nabla \lambda\|_{L^2}^2 + \int_{\Omega} q_s \lambda^2 \, dx \geq \|\nabla \lambda\|_{L^2}^2 \geq \frac{1}{1 + C_p^2} \|\lambda\|_{H^1}^2, \quad (\text{A.15})$$

where  $C_p$  is the Poincaré constant on  $H_{\diamond}^1(\Omega)$ . The right-hand side in (A.12) is bounded on  $H_{\diamond}^1(\Omega)$ . Therefore, by the Lax–Milgram theorem, there exists a unique  $\lambda(s) \in H_{\diamond}^1(\Omega)$  solving (A.12), and the bound  $\|\lambda(s)\|_{H^1} \leq C \|q_s\|_{L^2}$  holds.

Define

$$F : W^{1,\infty}(\Omega; \mathbb{R}^d) \times H_{\diamond}^1(\Omega) \rightarrow H^{-1}(\Omega), \quad F(\tilde{s}, \lambda) := -\Delta \lambda + q_{\tilde{s}} \lambda + Dq_{\tilde{s}},$$

with  $q_{\tilde{s}} = |\tilde{s}|^2 + \nabla \cdot \tilde{s}$ . Then  $F$  is continuously Fréchet differentiable. We further define

$$D_{\lambda} F(s, \lambda) = -\Delta + q_s : H_{\diamond}^1(\Omega) \rightarrow H^{-1}(\Omega),$$

which is associated with the bilinear form  $a_s$  by  $(D_{\lambda} F(s, \lambda)(\lambda), \varphi)_{L^2} = a_s(\lambda, \varphi)$  for all  $\lambda, \varphi \in H_{\diamond}^1(\Omega)$ . The coercivity of  $a_s$  implies that the operator  $D_{\lambda} F(s, \lambda)$  is a bounded linear isomorphism  $H_{\diamond}^1(\Omega) \rightarrow H^{-1}(\Omega)$ . Hence, by Theorem A.1, there exist a neighborhood  $U \subset W^{1,\infty}(\Omega; \mathbb{R}^d)$  of  $s$  and a  $C^1$  map  $\Lambda : U \rightarrow H_{\diamond}^1(\Omega)$  such that  $F(\tilde{s}, \Lambda(\tilde{s})) = 0$  for all  $\tilde{s} \in U$ , and  $\Lambda$  is locally Lipschitz in the  $H^1$ -norm:

$$\|\Lambda(\tilde{s}) - \Lambda(s)\|_{H^1} \leq C \|\tilde{s} - s\|_{W^{1,\infty}}.$$

From (A.11), for  $\tilde{s} \in U$  we have

$$\mathbf{v}^*(\tilde{s}) - \mathbf{v}^*(s) = \nabla(\Lambda(\tilde{s}) - \Lambda(s)) - \Lambda(\tilde{s}) \tilde{s} + \Lambda(s) s.$$

Taking the  $L^2$ -norm and using the uniform boundedness of  $\Lambda(\cdot)$  on  $U$  gives

$$\|\mathbf{v}^*(\tilde{s}) - \mathbf{v}^*(s)\|_{L^2} \leq C \|\Lambda(\tilde{s}) - \Lambda(s)\|_{H^1} + C \|\Lambda(s)\|_{L^2} \|\tilde{s} - s\|_{L^{\infty}} \leq C \|\tilde{s} - s\|_{W^{1,\infty}}.$$

This proves the claimed local Lipschitz continuity.  $\square$

**Remark A.1.** The condition  $q_s \geq 0$  is sufficient to ensure coercivity of the bilinear form  $a_s$  used in the proof. This can be relaxed to the weaker condition  $\|q_s^-\|_{L^{\infty}(\Omega)} < C_p^{-2}$ , where  $q_s^-(x) = \max\{-q_s(x), 0\}$  and  $C_p$  is the Poincaré constant for  $H_{\diamond}^1(\Omega)$ . Indeed, under this condition we have

$$|a_s(\lambda, \lambda)| \geq \|\nabla \lambda\|_{L^2}^2 - \int_{\Omega} q_s^- \lambda^2 \, dx \geq (1 - C_p^2 \|q_s\|_{L^{\infty}}) \|\nabla \lambda\|_{L^2}^2 \geq \frac{1 - C_p^2 \|q_s\|_{L^{\infty}}}{1 + C_p^2} \|\lambda\|_{H^1}^2,$$

so that  $a_s$  remains coercive. Hence, all conclusions of the theorem remain valid under this weaker condition.

With the lemmas established above, we are ready to prove Theorem 3.1.

*Proof of Theorem 3.1.* Under suitable conditions on the velocity field, Lemma A.1 justifies the regularity of the invariant density and thus the regularity of the score function. Given such a score function  $s$ , Lemma A.2 establishes the existence and uniqueness of a minimizer  $v^*$  for problem (A.7). Lemma A.3 shows that the solution map  $s \mapsto v^*$  is locally Lipschitz continuous from  $W^{1,\infty}(\Omega; \mathbb{R}^d)$  into  $L^2(\Omega; \mathbb{R}^d)$ , which yields the stability assertion. This completes the proof of the theorem.  $\square$